JOURNAL OF PETROLOGY

Journal of Petrology, 2015, Vol. 56, No. 11, 2195–2222
doi: 10.1093/petrology/egv069
Original Article

OXFORD

Trapped Liquid, Paleo-porosity and Formation Time Scale of a Chromitite–(Ortho)pyroxenite Cumulate Section, Bushveld, South Africa

Shahrzad Manoochehri[1]*, Max W. Schmidt[1] and Wimpie Britz[2]

[1]Institute of Geochemistry and Petrology, Department of Earth Sciences, ETH Zurich, Clausiusstrasse 25, 8092 Zurich, Switzerland and [2]Modikwa Platinum Mine, 292KT Onverwacht Hill, Steelport Region, Mpumalanga South Africa

*Corresponding author. E-mail: shahrzad.manoochehri@alumni.ethz.ch

Received January 30, 2015; Accepted November 6, 2015

ABSTRACT

To evaluate compaction and interstitial melt expulsion during cumulate formation, a 20 m cumulate section including the UG2 and UG3 chromitites from a 264 m drill core through the Upper Critical Zone of the Bushveld Complex (South Africa) has been studied. The cumulates in the studied section are as follows: 3 m plagioclase pyroxenite to pyroxenite, pegmatoid footwall pyroxenite at the lower contact to UG2, 0·7 m UG2 chromitite, 6·8 m pyroxenite, 0·24 m UG3 chromitite, 2·0 m plagioclase-rich pyroxenite changing locally to norite, the two 5 cm leader stringers UG3a and UG3b, and 7 m total of olivine pyroxenites grading into plagioclase pyroxenites. All pyroxenites are dominated by orthopyroxene (opx) and the cumulate sequence is topped by mottled anorthosite grading into norite. Stratigraphic concentrations of major and trace elements of 52 bulk-rock samples were determined. Bulk-rock Mg-numbers are 0·79–0·81 throughout the silicate cumulate units, and 0·40–0·46 in the chromitite layers. The stratigraphic distribution of six incompatible trace elements (K, Rb, Ba, Cs, Zr and Th) has been used to determine the amount of trapped liquid (F_{TL}) or paleo-porosity in the cumulate rocks. Final porosities (volume fractions), based on averages from the six trace elements, are 0·06–0·33 in the pyroxenites. In chromitite layers, trapped melt fractions of 0·12–0·36 are calculated from incompatible trace element concentrations, but bulk SiO_2 concentrations and X-ray tomography yield 0·04–0·17 higher porosities. Hence, the bulk silicate fraction in the chromitites may not necessarily correspond to the trapped liquid fraction, as poikilitic opx was crystallizing while the silicate melt still equilibrated. Using a previously derived experiment-based model for compaction time scales, gravitationally driven chemical compaction in the UG2–UG3–pyroxenite section is calculated to occur within 1–10 years. This time frame corresponds to the times necessary to cool a 20 m layer by 10–50°C, the temperature interval argued to encompass the liquidus and almost complete solidification. Compaction within a decade can in fact easily develop the paleo-porosities indirectly observed today and is probably stopped by crystallization of the interstitial liquid. Contrary to previous assertions, melt expulsion from the cumulate pile does not hinder compaction; calculated permeabilities would allow for the migration of an order of magnitude higher amount of melt than has to be expelled from the 20 m pile of cumulate. The pegmatoid zones in the chromitite footwalls enriched in incompatible trace elements are consistent with a collection of interstitial melts expelling from the underlying compacting pyroxenites. Their entrapment below the chromitite layers suggests that these act as permeability barriers. This is in part due to their finer grain size compared with the pyroxenites, but is mainly due to the crystallization of large poikilitic opx during compaction.

Key words: chromitite; compaction; layered mafic intrusions; paleo-porosity

INTRODUCTION

Large Layered Mafic Intrusions (LMIs) such as the Bushveld Complex, South Africa, preserve evidence for cumulus and post-cumulus processes occurring in magma chambers and crystal mushes (e.g. Sparks *et al.*, 1985). Cumulates are conventionally characterized by the presence of an interstitial melt preserved between the cumulate grains (Wager *et al.*, 1960; Wager & Brown, 1968). Newly formed crystal mushes typically have initial melt contents of 50–70% (e.g. Campbell, 1978; Irvine, 1982; Shirley, 1987; Naslund & McBirney, 1996; Tegner *et al.*, 2009) but in most cases some interstitial melt escapes, percolating upwards through the cumulate pile. Among different mechanisms, gravitationally driven compaction has been proposed as the main driving force for expulsion of interstitial liquid (e.g. McKenzie, 1984; Sparks *et al.*, 1985; Shirley, 1987; Meurer & Boudreau, 1996, 1998*a*; Philpotts *et al.*, 1996; Mathez *et al.*, 1997; Boorman *et al.*, 2004; Tegner *et al.*, 2009; Namur & Charlier, 2012). The upward escape of interstitial melt owing to compaction remains efficient until the melt becomes trapped because of cooling, textural evolution of the framework minerals (e.g. Hunter, 1996), or the presence of a relatively impermeable layer on top of the compacting cumulates (e.g. Mathez *et al.*, 1997). Short solidification times in comparison with compaction times are thought to constitute the main obstacle for the efficiency of the compaction process (e.g. Irvine, 1970*b*). Permeability barriers, hindering melt percolation, may form as a result of differential compaction in the crystal mush caused by differences in mineral types, grain size and modes of the crystal matrix (e.g. Mathez *et al.*, 1997; Mathez & Mey, 2005).

The above processes are documented in the textural, lithological and geochemical characteristics of the cumulate rocks (e.g. Boudreau & McBirney, 1997; Meurer & Boudreau, 1998*a*, 1998*b*; Mathez & Mey, 2005). As an example, the amount of the remaining melt (i.e. the trapped liquid fraction or residual porosity) is widely studied as an important measure for evaluating the effectiveness of post-cumulus compaction (e.g. Henderson, 1968; Barnes, 1986; Cawthorn & Walsh, 1988; Meurer & Boudreau, 1996, 1998*a*; Mathez *et al.*, 1997; Meurer & Meurer, 2006; Tegner *et al.*, 2009; Namur & Charlier, 2012).

To evaluate compaction in cumulates we present a detailed geochemical profile and calculated trapped liquid contents through a part of the Upper Critical Zone of the Bushveld Complex. From a 264 m drill core we studied a 20 m section in detail, comprising the UG2 and UG3 chromitite layers, their footwall rocks and their hanging-wall pyroxenites. The chromitite layers are of special interest, not only because of their economic importance but also because they preserve evidence of post-cumulus processes (e.g. Mathez & Mey, 2005). Variations in their texture, lithology and geochemistry contribute to an understanding of processes occurring after deposition of the chromite (e.g. Hulbert & von Gruenewaldt, 1985; Mathez & Mey, 2005; Vukmanovic *et al.*, 2013). The presence of pegmatoid rocks in the footwall of UG2 is interpreted as one of these features; however, despite extensive textural and geochemical studies (e.g. Viljoen & Scoon, 1985; Viljoen *et al.*, 1986; Cawthorn & Barry, 1992; Mathez & Mey, 2005; Voordouw & Beukes, 2009) it is still debated if the pegmatoid texture is the result of liquid expulsion during compaction or injection of new magma.

To determine the amount of trapped liquid, a detailed trace element concentration profile was acquired in this study and the suitability of individual incompatible trace elements for determining paleo-porosities evaluated. The paleo-porosity profiles from the drill core and their effective compaction times are then modeled on the basis of previous experiments on the compaction time scales of silicate and chromitite layers (Schmidt *et al.*, 2012; Manoochehri & Schmidt, 2014).

GEOLOGICAL SETTING OF THE BUSHVELD COMPLEX

The Bushveld Complex, the world's largest layered mafic intrusion, was intruded into the upper part of the 2·1–2·3 Ga Pretoria Group, part of the Transvaal Supergroup (e.g. Barnes & Maier, 2002). Based on the South African Commission for Stratigraphy (SACS, 1980) the Complex is composed of three units: (1) the Rustenburg Layered Suite (RLS); (2) the granophyres and granites overlying the RLS known as Rashoop Granophyre Suite; (3) the Lebowa Granite Suite. The Rustenburg Layered Suite has an ~60 000 km^2 subsurface area and is 7–9 km in thickness (e.g. Eales & Cawthorn, 1996; Maier *et al.*, 2013). The importance of the Bushveld Complex is not limited to its petrological characteristics as a layered intrusion, but includes also its economic significance, hosting almost the bulk of global resources in platinum group elements (PGE), chromium and vanadium, together with valuable resources of copper, nickel, gold and iron (e.g. Maier *et al.*, 2013). These metals are either major elements in distinct mineral layers (e.g. Cr, V and Ti in chromitite or magnetite layers) or trace elements in specific cumulate horizons (e.g. PGE in base metal sulfides in chromitites and pyroxenites).

Outcrops of the Bushveld Complex are grouped in four regions: the Eastern, Western, Northern or Potgietersrus and Far Western lobes (or limbs) (e.g. Eales & Cawthorn, 1996; Maier *et al.*, 2013) (Fig. 1). In the southeastern part of the complex, a fifth hidden lobe covered by sediments is thought to be present (Eales & Cawthorn, 1996). The direct connection of these lobes at depth is still a matter of debate, but the similarities in stratigraphy and gravity models, especially in the Western and Eastern lobes, suggest a continuous magma chamber for these outcrops (Cawthorn & Webb, 2001).

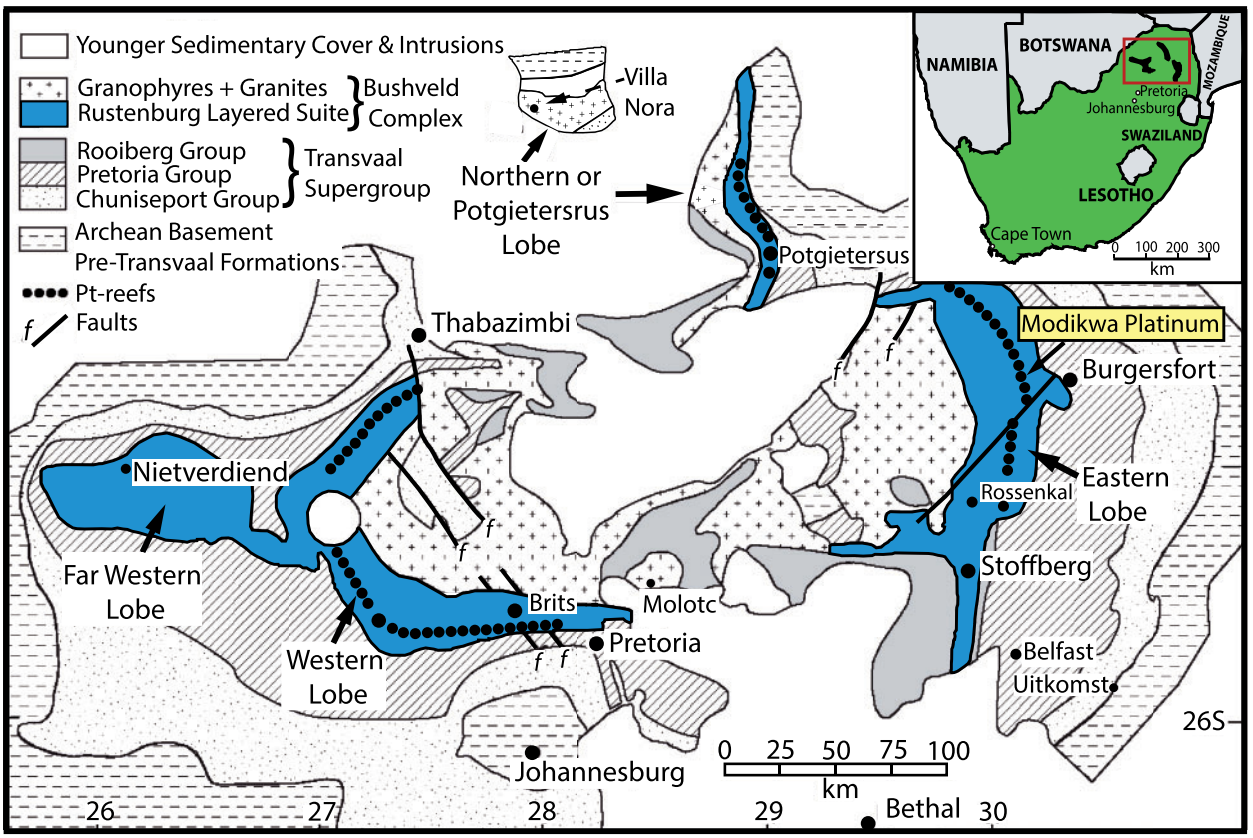

Fig. 1. Geological map of the Bushveld Complex and its country rocks (adapted from Barnes & Maier, 2002). Location of the Bushveld Complex is marked with a red square in the inset. The drill core studied here is from the Modikwa Platinum Mine.

Stratigraphy of the Bushveld Complex

The mafic to ultramafic layered series present in different lobes are divided into five stratigraphic zones: Marginal Zone, Lower Zone (LZ), Critical Zone (CZ), Main Zone (MZ) and Upper Zone (UZ) (Fig. 2a) (Eales & Cawthorn, 1996). The Critical Zone is of special interest because of its chromite- and PGE-enriched cumulate layers (e.g. UG2, Merensky reef and Platreef) and is divided into two subzones, the Lower Critical Zone (L_CZ) and the Upper Critical Zone (U_CZ). The L_CZ is mainly composed of orthopyroxenite and the U_CZ contains interbeddings of mainly norite and orthopyroxenite. The U_CZ is characterized by the first appearance of plagioclase as a cumulus mineral and the occurrence of cyclic units (e.g. Eales & Cawthorn, 1996). In most areas U_CZ consists of eight cyclic units of chromitite, pyroxenite and norite. Some units contain anorthosite at the top and not all contain chromitite (Barnes & Maier, 2002).

The chromitite layers are mostly located in a stratigraphic interval spanning in total 800–1000 m and are classified in three stratigraphic groupings known as the lower, middle and upper groups with numbers referring to single layers within each group (Cousins & Feringa, 1964). Thus from the base of the upper group, UG2 is the second layer of chromitite, which in most localities is a massive, 60–110 cm thick layer with 75–90 vol. % chromite (e.g. Eales, 1987; Mathez & Mey, 2005; Mondal & Mathez, 2007). This layer occurs throughout almost the entire Bushveld and is probably, worldwide, the most extensive single cumulate layer. In contrast, the UG3 chromitite layer is limited to the central Eastern sector of the Bushveld Complex and is not observed in the Western lobe (Hatton & von Gruenewaldt, 1987).

Parental magma of the Bushveld Complex

Estimating the magma parental to the Bushveld Complex, or more specifically to the Rustenburg Layered Suite, has been the topic of numerous studies (e.g. Cawthorn & Davies, 1983; Sharpe & Hulbert, 1985; Cawthorn, 2007; Barnes *et al.*, 2010; Godel *et al.*, 2011). The proposed parental magma compositions are mainly based on the whole-rock compositions of chilled marginal zones and of sills or dykes at contacts between different zones or at the floor of the intrusion. Three magma types, named B1, B2 and B3 (Bushveld 1–3, Supplementary Data Electronic Appendix 1; supplementary data are available for downloading at http://www.petrology.oxfordjournals.org), have been proposed as the parental liquids of different zones of the intrusion: B1 is a basaltic andesite or high-silica, high-magnesium basalt with a crystallization sequence similar to the Lower and Lower Critical Zone; B2 and B3 are similar to tholeiitic basalts and their compositions are

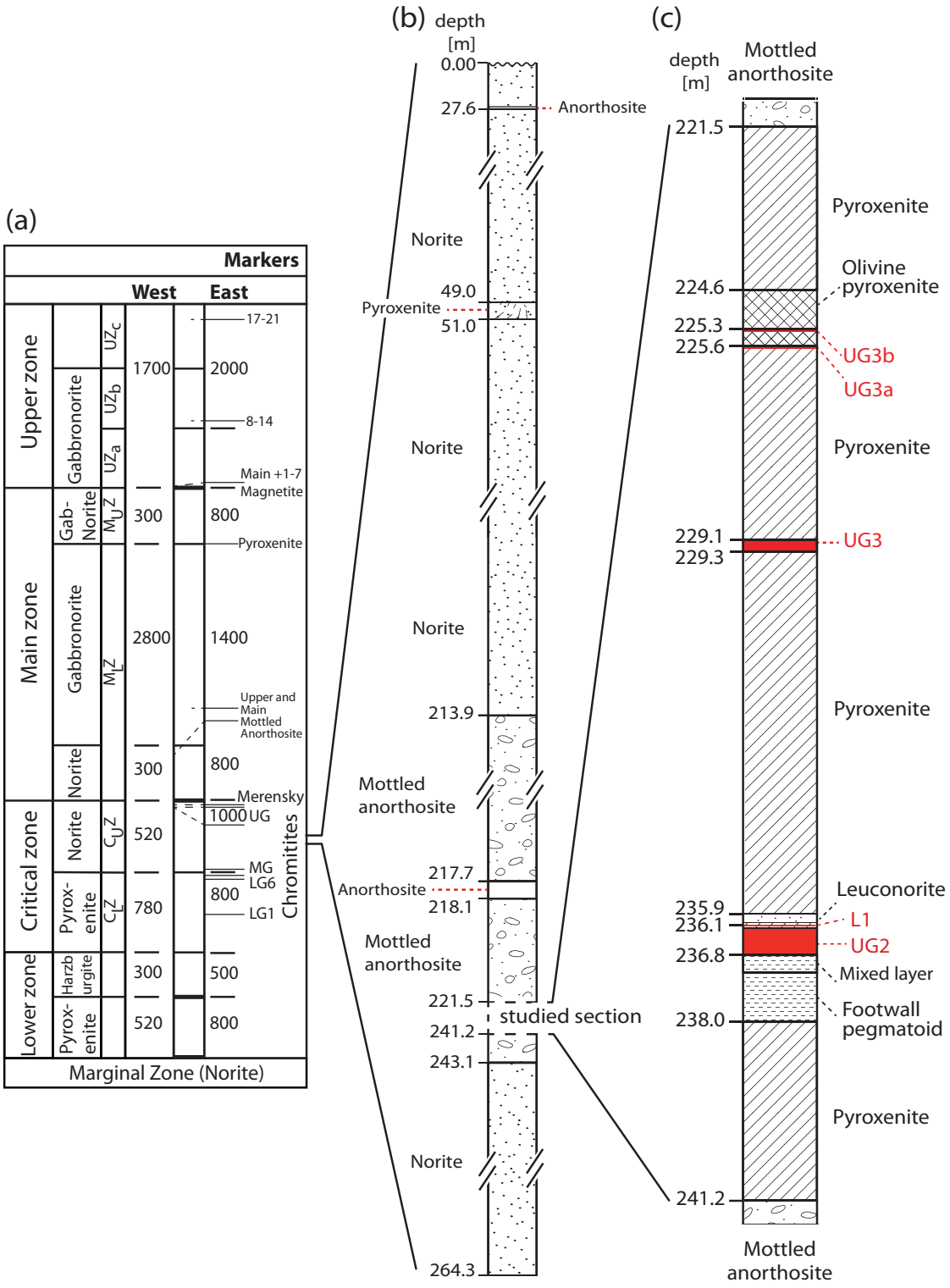

Fig. 2. (a) Generalized stratigraphic section through the Eastern and Western lobes of the Bushveld Complex showing the appearance of cumulus phases (after Eales & Cawthorn, 1996; Van der Merwe & Cawthorn, 2005). LG, Lower Group chromitites; MG, Middle Group chromitites; UG, Upper Group chromitites; numbers 1–21 in the Upper Zone refer to magnetite layers. (b) Stratigraphy of the entire drill core from the Modikwa Platinum Mine. (c) Stratigraphy of the 20 m of the drill core studied in detail.

derived from rocks in contact with the Upper Critical Zone and Main Zone, respectively. However, Barnes *et al.* (2010) have determined that the crystallization sequence of the B2 magma does not match with that of U_CZ and despite its stratigraphic position it cannot be parental to this zone. Instead, a 60:40 mixture of B1–B2 magmas has been suggested to have a composition that can reproduce the crystallization sequence of the

Upper Critical Zone (Barnes *et al.*, 2010; Godel *et al.*, 2011).

THE DRILL CORE

The 264 m drill core (Fig. 2b) of 2 inch diameter intersects the Upper Critical Zone in the central Eastern lobe; access was provided by Modikwa Platinum Mine for this study. The Modikwa mine is located ~25 km NW of Burgersfort (Fig. 1), along the border between the Mpumalanga and Limpopo provinces. The 20 m section of the core studied here in detail contains all cumulates associated with the UG2 and UG3 chromitites (Fig. 2c); the other 244 m consists of extensive lengths of gabbronorite, norite and several anorthosites. The interval of detailed investigation starts with the mafic unit directly below the UG2 chromitite (241·2 m depth), continues up-section through UG2 and its leader stringer (L1), followed by overlying pyroxenites, then UG3, UG3a and b, with their hanging-wall olivine pyroxenites and pyroxenites (to 221·5 m depth). The detailed lithology of the studied core section is shown in Fig. 2c and described below.

Complete stratigraphy of the drill core

The 264 m drill core (Fig. 2b) starts at its base with 21 m of norite composed of plagioclase and orthopyroxene (opx) with minor amounts of clinopyroxene (cpx). Local variations in grain size, from millimeter to centimeter scale, are a common feature throughout the layer. This thick noritic layer grades upwards into mottled anorthosite, extending for 1·9 m and composed of >85 vol. % plagioclase with intercumulus opx and cpx appearing as large mottles. The mottled anorthosite is overlain by a 19·8 m succession of pyroxenites (or melanorites) and chromitite layers (UG2 and UG3), forming our detailed section (Fig. 2c). The ultramafic cumulate succession is overlain by mottled anorthosite, which continues upwards for 7·6 m and has local variations to spotted anorthosite or leuconorite. Spotted anorthosite consists of >85 vol. % plagioclase and contains dark spots of opx and relatively minor cpx, which are evenly spaced and occur in small poikilitic patches. These rocks are sometimes termed anorthositic norites (Klerk, 1995). The mottled anorthosite layer is then overlain by 213 m of norite, typically with 20–30 vol. % opx with local variations in plagioclase content (to <10 vol. % pyroxene, i.e. leuconorite to anorthosite) and grain size (mm to cm scale). At 51 m depth the norite is interrupted by a 1·2 m thick pyroxenite layer; this layer grades upwards into a noritic composition similar to its footwall lithology.

Stratigraphy of the UG2–UG3 cumulate section

The UG2–UG3 cumulate section is mostly composed of chromitite and pyroxenite. The latter rocks are dominated by opx, but in some layers olivine, cpx or plagioclase may become abundant, such that these rocks are nominally almost never orthopyroxenites but pyroxenites. In these pyroxenites (except for the pegmatoids), plagioclase is always interstitial and its mode mainly reflects the amount of intercumulus melt.

UG2 footwall pyroxenite

The key part of the studied drill core section starts with an almost 3 m thick layer of plagioclase pyroxenite (or melanorite) known as the footwall pyroxenite (Fig. 2c) (Mathez & Mey, 2005; Mondal & Mathez, 2007). This rock consists of 70–80 vol. % granular to tabular, euhedral to subhedral opx with grain sizes of 1–3 mm. Intercumulus plagioclase constitutes 10–30% of the rock and, as in all other pyroxenites, is xenomorphic, has a grain size distinctly smaller than the pyroxenes, generally lacks optical zoning, and mostly forms plates in interstitial spaces (Fig. 3a). Throughout the entire layer, the amount of plagioclase changes locally and may be <10 vol. %. Chromite is scarce except in the top part of the layer close to the chromite-rich mixed layer unit. Locally, throughout the footwall pyroxenite, large (1–2 cm) oikocrysts of cpx are observed.

UG2 footwall pegmatoid

The UG2 footwall pyroxenite grades into an almost 1 m thick pegmatitic layer with local variations in mineral mode and texture. The most prominent variation is an ~20 cm thick zone, composed of 2–4 cm subhedral to sub-rounded opx grains and centimeter-sized plagioclase as an interstitial phase (Fig. 3b). Sub-rounded to euhedral chromite is always present in this layer. Relatively high amounts of amphibole and phlogopite (up to 10 vol. %) are observed interstitially as late crystallizing phases. The mineralogy and textural characteristics of this part of the sequence are similar to those of the footwall pegmatoid or pegmatoid pyroxenites described in the literature (e.g. Mathez & Mey, 2005). However, variations in grain size and mode are not limited to this coarse-grained 20 cm layer but continue upwards; local enrichments in phlogopite and amphibole as interstitial phases are observed throughout the entire thickness of this layer (Fig. 3c).

Mixed layer

The footwall pegmatoid is directly overlain by a 30 cm thick layer of olivine-bearing plagioclase pyroxenite, similar to the 'mixed layer' described by Mathez & Mey (2005). This rock consists of 70–80% subhedral, coarse-grained (2–3 cm) cumulate opx and interstitial plagioclase. Partly serpentinized anhedral olivine grains are locally present and surrounded by megacrysts of opx (Fig. 3d). Characteristic for this layer is abundant chromite, which appears as irregular patches or layers on a centimeter scale. Most disseminated chromite or small chromite patches are poikilitically overgrown by opx or plagioclase. Together with plagioclase, phlogopite and amphibole are the main interstitial minerals; in some parts of the mixed layer, chromite is overgrown by

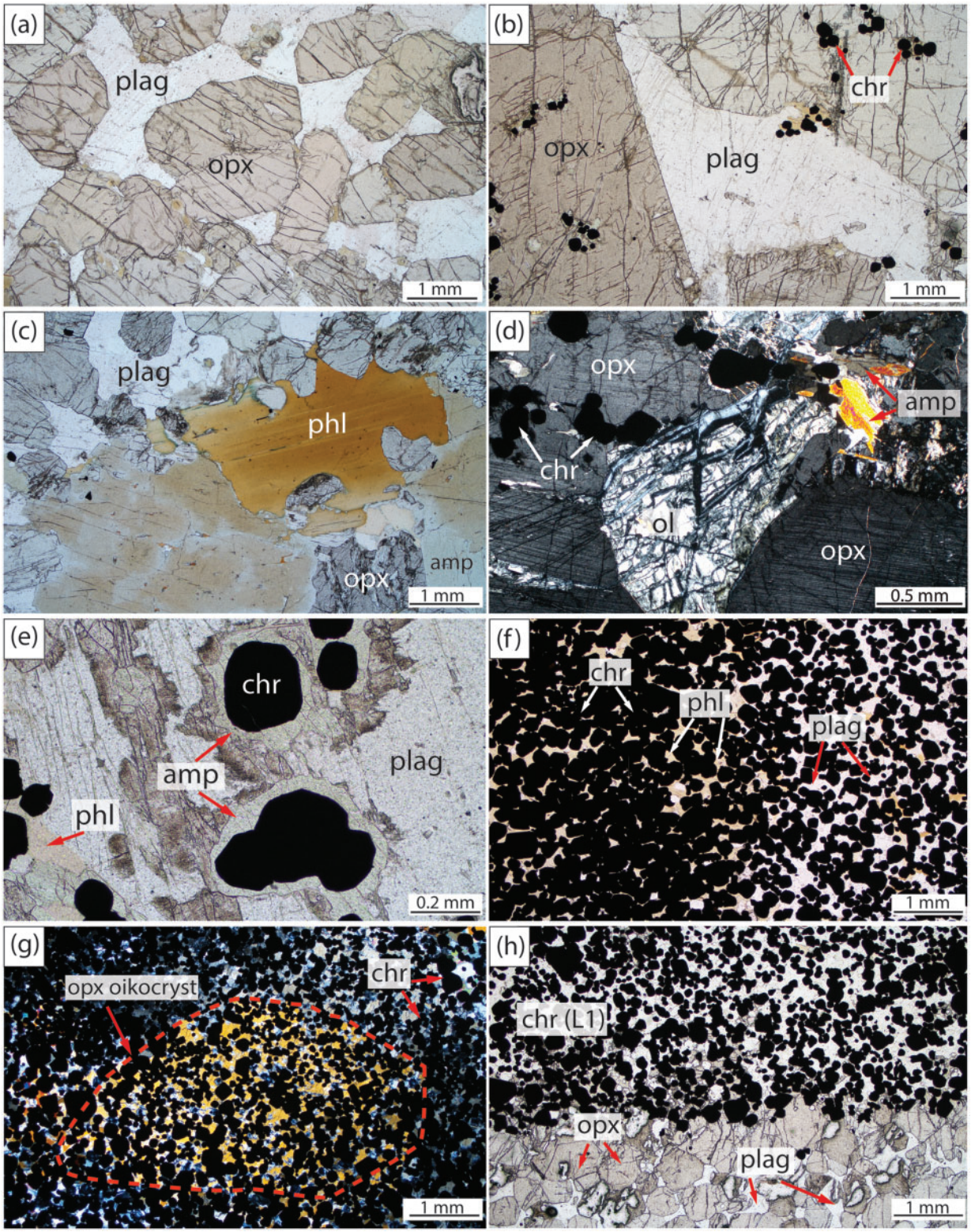

Fig. 3. Photomicrographs illustrating the petrographic characteristics of the main units in the studied drill core. (a) Common footwall pyroxenite with granular, subhedral orthopyroxene (opx) and interstitial plagioclase (plag); plane-polarized light. (b) Footwall pegmatoid with centimeter-scale orthopyroxene (opx) and interstitial plagioclase (plag) and sub-rounded to euhedral chromite (chr) grains; plane-polarized light. (c) Local enrichments in phlogopite (phl) and amphibole (amp) are commonly observed in UG2 footwall pegmatoid; plane-polarized light. (d) In the mixed layer just below UG2 partly serpentinized olivine (ol) crystals surrounded by opx megacrysts (opx) are locally observed; crossed Nicols. (e) In some portions of the mixed layer, chromite (chr) is overgrown by amphibole (amp); plane-polarized light. (f) UG2 chromitite with 71–85% modal chromite (chr) and wide grain-size distributions; plane-polarized light. (g) Poikilitic opx in the UG2 chromitite; crossed Nicols. (h) Sharp contact between the leader stringer (L1) and its footwall unit; plane-polarized light.

amphibole (Fig. 3e). The upper contact of the mixed layer is against the UG2 chromitite.

UG2 chromitite

UG2 is a massive, ~70 cm thick layer containing 70–85 vol. % chromite (Fig. 3f) with euhedral to rounded shapes. Grain sizes vary between 0·03 and 2 mm, but most grains are ~0·1–0·3 mm. Coarse grains are either evenly distributed within a matrix of finer ones or are concentrated in patches or bands that are distinct from the fine-grained areas (Fig. 3f). Chromite with a range of size distributions has been reported by Mathez & Mey (2005) in UG2 samples from the Northeastern Bushveld, by Hulbert & von Gruenewaldt (1985) in UG2-like chromitite layers in the Northwestern Bushveld and by Eales (1987) in chromitite layers in the Western Bushveld. The contact between the mixed layer and the UG2 chromitite layer is irregular, at least on the limited width of the studied drill core.

Arrangements of fine chromite grains in chain structures are often observed. Some large chromite crystals contain silicate inclusions. This feature has been interpreted as the result of either sintering of finer grains and entrapping of interstitial minerals as inclusions (Hulbert & von Gruenewaldt, 1985), or deformation of grains during cumulate compaction (Vukmanovic *et al.*, 2013). Interstitial minerals can be texturally divided into two groups: first, large to medium-sized (mm to cm scale) opx and plagioclase oikocrysts growing over chromite grains (Fig. 3g); second, medium to fine grains (μm to mm scale) of mostly plagioclase, phlogopite and amphibole (Fig. 3f).

UG2 up-section

The UG2 chromitite is overlain by an ~18 cm thick succession of several thin layers, starting with a 0·8 cm layer of fine-grained (0·2–0·5 mm) plagioclase pyroxenite, changing with a sharp contact (Fig. 3h) to a 1·0 cm thick layer of massive chromitite, corresponding to the first leader stringer (L1). Three thin chromitite layers, variously known as 'leaders', 'markers' or 'triplets', have been reported within a 10–100 cm interval above UG2. These layers are 1–2 cm thick and have been described to bifurcate and merge with each other or with UG2 (e.g. Viljoen *et al.*, 1986; Mathez & Mey, 2005).

The leader stringer (L1) observed in the studied core is overlain by a 6 cm fine- to medium-grained (0·5–1 mm) plagioclase pyroxenite with 10–15% plagioclase in its lower part. Upwards this layer becomes gradually coarser grained (2–3 mm), with less plagioclase (<5%) and more phlogopite and amphibole in its top 2 cm. A very thin chromitite stringer (possibly leader stringer L2) separates this layer from an ~10 cm leuconorite layer (Fig. 4a). This layer consists of ~70–80 vol. % subhedral plagioclase laths (0·5–0·8 mm) and 20–30 vol. % opx and grades upwards into an anorthositic (<5 vol. % opx) layer in its top few centimeters. All of these sublayers have sharp contacts with each other.

UG2 hanging-wall pyroxenite

Above UG2 is the hanging-wall pyroxenite (melanorite), a 6·6 m thick layer mineralogically identical to the footwall pyroxenite, but with local differences in texture and mineral modes. Pyroxene grain sizes mostly range from fine to medium (0·5–3·0 mm), but locally coarser zones are also observed. Plagioclase is xenomorphic, almost never shows any zonation under the optical miscroscope, is mostly smaller than the pyroxenes, and is interpreted as an intercumulus phase. Locally, large cpx oikocrysts enclose opx. Chromite is present only in the first few meters above the UG2 chromitite and becomes scarce to absent in the top part of the layer. Phlogopite and amphibole are the two main accessory minerals; their abundance varies locally between 1 and 5 vol. % throughout the layer. These observations are similar to the characteristics of the hanging-wall pyroxenite reported by Mathez & Mey (2005) and Mondal & Mathez (2007). Just below UG3, there is a zone of more coarse-grained, almost pegmatoid pyroxenite enriched in interstitial phlogopite and amphibole.

UG3 chromitite

On top of the hanging-wall pyroxenite, 6·8 m above UG2, the third upper group chromitite appears (Figs 2c and 4b). The lower pyroxenite has a moderately sharp contact with the UG3 chromitite layer. UG3 is 24 cm thick and similar to UG2 but contains less chromite (60–75 vol. %) and has generally finer grains (0·05–0·5 mm) (Fig. 4b). Chromites are enclosed in large oikocrysts of opx and plagioclase. A few per cent (3–4 vol. %) phlogopite and amphibole occur as fine-grained interstitial phases (Fig. 4b). The upper contact of UG3 is irregular; however, the limited core diameter does not allow any detailed investigation of this contact.

UG3 hanging wall

The hanging wall of UG3 is a medium-grained 3·5 m thick plagioclase-rich pyroxenite varying locally to melanorite. Chromite is generally present and ranges in volume from 2 to 15%. Phlogopite and amphibole are the main accessory minerals and their contents vary through the layer, although remaining at <2 vol. %.

UG3a chromitite

Above the pyroxenite is an 8 cm thick chromitite stringer known as UG3a. UG3a is a dense layer with 80–95% chromite. Similar to UG2, on a thin-section scale, there are areas with variable chromite concentrations and grain-size ranges. Interstitial phases are mostly phlogopite, plagioclase and opx. The lower and upper contacts of this chromitite layer are relatively sharp.

UG3a hanging-wall olivine-pyroxenite

The hanging wall of UG3a is a coarse-grained (mm to cm scale) olivine pyroxenite (melanorite), which grades into plagioclase-bearing harzburgite up-section (Fig. 4c). The harzburgite contains opx and up to 30 vol.

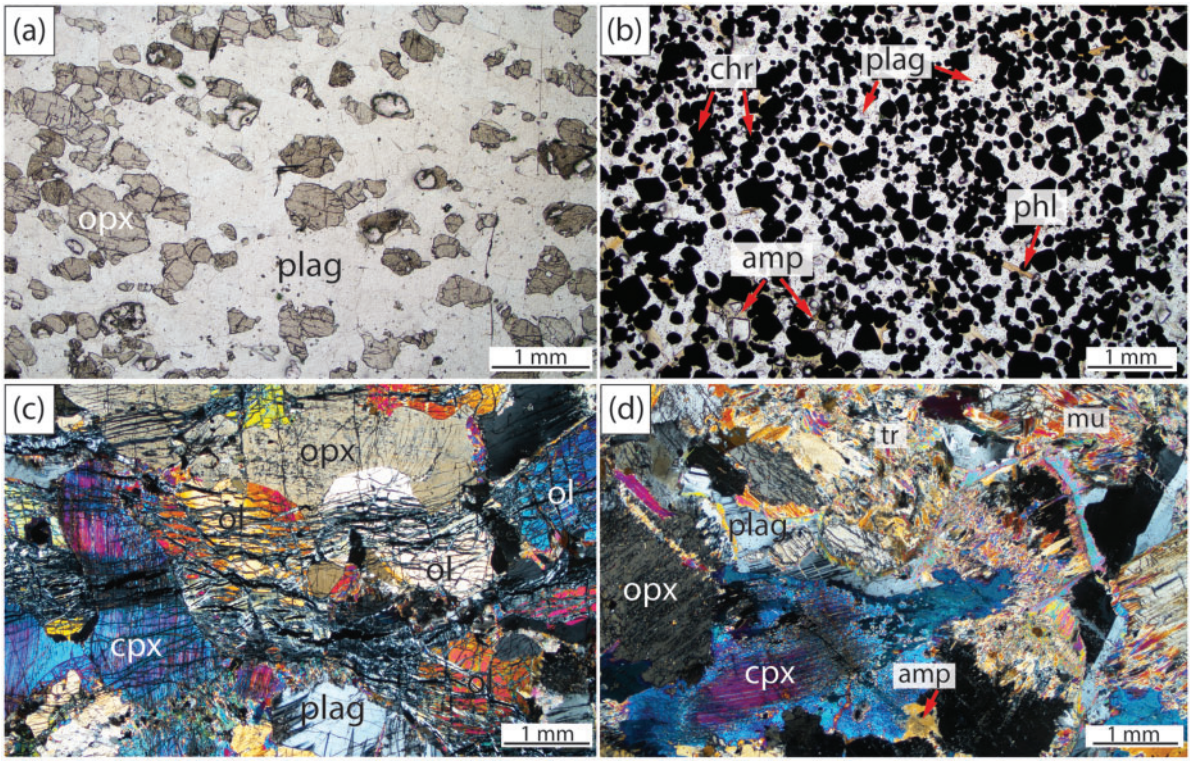

Fig. 4. (a) Leuconorite at the upper contact of a thin chromitite stringer (possibly L2); plane-polarized light. (b) UG3 chromitite with ~60 vol. % chromite and with plagioclase (plag), phlogopite (phl) and amphibole (amp) as interstitial phases; plane-polarized light. (c) Plagioclase-bearing harzburgite in the hanging wall of UG3a and UG3b chromitites; crossed Nicols. (d) Altered sample within UG3b hanging-wall pyroxenites, at greenschist facies, containing large amount of tremolite (tr), muscovite (mu) and amphibole (amp); crossed Nicols.

% partly serpentinized olivine as cumulus minerals, both typically 1–2 mm in size (Fig. 4c). Phlogopite and amphibole are the main accessory minerals. Chromite is always present.

UG3b chromitite

Some 28 cm above UG3a, within the olivine-rich cumulates, another chromitite stringer occurs, known as UG3b. In the studied core, UG3b is composed of one 6 cm thick massive chromitite and an assemblage of several thin chromitite layers with different grain sizes (0·05–0·5 mm) and locally different chromite contents. In some areas chromite reaches almost 100% modal abundance, whereas in other parts chromite is so disseminated that it can hardly be recognized as a distinct layer. Such characteristics have also been reported for UG2 leaders in other localities in the Eastern Bushveld (Mathez & Mey, 2005).

UG3b hanging wall

UG3b is overlain by an ~65 cm layer composed of a plagioclase-bearing harzburgite in its lower part similar to the UG3b footwall rock. Up-section this layer grades into a coarse-grained (0·7–1 mm) plagioclase pyroxenite similar to the UG3 hanging wall. The pyroxenite layer extends for almost 3 m. It terminates with a relatively sharp contact against a mottled anorthosite (Fig. 2b and c).

Secondary alterations and late-stage dikes

Within the UG3 hanging-wall pyroxenites local macroscopic alteration minerals of greenschist-facies grade can be observed. In such samples high amounts of muscovite, tremolite, actinolite, chlorite, saussuritized plagioclase and quartz are present (Fig. 4d). As described below, one of the analyzed samples from the UG3b hanging-wall pyroxenites turned out to be altered. In this sample (MP-222·93) the greenschist-facies minerals could be observed in thin section but were not obvious in the hand specimen.

Throughout the 264 m drill core, a few centimeter-wide dikes or dikelets occur. These are mainly composed of anorthosite with minor amount of amphibole and phlogopite. Chromite and zoisite are also locally present. These dikes have sharp borders cutting the host-rock minerals and represent late-stage intrusions. There is no evidence of alteration by fluids in the vicinity of these dikelets. In contrast to the pegmatoids, there is no apparent interaction with the host-rock; nevertheless, their vicinity was avoided during sampling.

METHODS

A total of 64 samples was selected across the entire core, of which 52 samples were from the UG2–UG3 ultramafic section. A denser sample spacing (1 cm or

less) was used for the chromitite layers. The samples used for bulk-rock analysis were generally the same as for thin sections, from which we determined the mineralogy, texture and grain size. Samples always reached across half the width of the core and their thickness was varied with respect to apparent crystal size and heterogeneity, such that representative chemical analyses were obtained.

Samples were crushed with a hydraulic stainless steel piston and those with no or minor chromite content were pulverized in an agate mortar for less than 10 min. Chromitites or chromite-rich samples were pulverized in planetary agate mills for 30–60 min. The mills were cleaned between each sample by grinding or milling a quartz sand–water mixture for 2 min. The powdered samples were dried for 24 h at 110°C.

To prepare lithium tetraborate (Li_2BO_4) glass discs, sample powders were heated at 1050°C for 2 h to determine the loss or gain on ignition (LOI or GOI). The fired products were mixed with Li_2BO_4 in weight ratios of 1:5 for felsic and chromite-poor mafic rocks, 1:10 for chromite-rich rocks and 1:50 for chromitite rocks. These different ratios were necessary to guarantee complete dissolution of chromite into the silicate–borate glass; each glass was carefully checked for homogeneity using a microscope. Fusing was done using an automated rotating Bunsen burner at 1000–1200°C and a fusion time of 10–30 min. Samples that remained optically heterogeneous even after 30 min fusion time were discarded and the sample–borate ratio was changed.

Major elements were analyzed by X-ray fluorescence (XRF) using a PANalytical Axios spectrometer operating at conditions of 20–100 kV and 24–100 A. Ultramafic samples underwent a specific background correction because of interferences or overlap between the Mg (Kα) and Na (Kα) peak positions, leading to artificially elevated Na concentrations in rocks with high Mg content.

Trace element abundances (including P) were determined by laser ablation inductively coupled plasma mass spectrometry (LA-ICP-MS) using a Nu Plasma 1700 ICP-MS system connected to a Lambda Physics 193 nm excimer laser ablation unit. Freshly broken surfaces of the glass discs employed for XRF analysis were used for these measurements. Pure Li_2BO_4 glass and NIST 610 were used as standards and were regularly reanalyzed for calibration. Three to eight ablation spots per sample, with 90 μm crater size, an ablation time of 60 s and a repetition rate of 10 Hz were used. Data reduction and concentration calculations were carried out with the SILLS program version 1.3.2 (Guillong *et al.*, 2008) using CaO as internal standard for silicate-dominated samples, and Al_2O_3 for chromitite samples.

Normative mineral contents of the silicate-dominated samples were calculated from a modified CIPW norm, ideally suited for the low-pressure, almost anhydrous mineralogy of the Bushveld. The modification concerns the amount of chromite, which was simply calculated by subtracting a real chromite composition (from UG2, Table 1) from the bulk-rock and then applying the CIPW norm calculation to a Cr-free composition. For the chromitites we have attempted the same method such that the normative mineral modes of the silicate matrix could be calculated. However, this correction is too sensitive to the exact chromite composition and does not work well even for the sample in which the chromite was analysed, yielding no feldspar, normative nepheline and all Ca in cpx. We have hence used the following normalization scheme. K, Na, and Ca are placed into feldspars. From the remaining Si, we calculate opx amounts. Then the amount of chromite, ulvöspinel and spinel–hercynite endmembers are calculated and the remaining Fe and Mg are recalculated as the magnetite–magnesioferrite endmember. It should be noted that the chromitites do not contain cpx and hence all Ca is placed into anorthite (both have the same Ca:Si ratio). With this method a correct mineral assemblage and realistic X_{An} (0·7–0·9) result, albeit with opx contents lower than observed. This is most probably a direct consequence of using feldspars as K, Na, and Ca hosts, whereas in the chromitite samples significant fractions of these elements are hosted by the low-Si phases phlogopite and amphibole.

To study the 3D distribution and proportions of silicates and chromite in the chromitites, X-ray computed tomography (X-ray CT) was applied to two samples from UG2 and UG3. Cylindrical samples with a diameter of 5 mm were drilled using a coring drill. These samples were scanned at ETH Zurich (Department of Environmental Systems Science) using a phoenix v|tome|x s 240 X-ray scanner (GE Sensing & Inspection Technologies GmbH, Germany). The acquisition parameters were set such that only two types of minerals were distinguished, the chromite and all other (silicate) minerals. These parameters are as follows: scanning resolution: 10 μm voxel edge length; current: 75 μA; voltage: 130 kV; number of images: 3200; exposure time per image: 200 ms. Volume reconstruction was performed using the software datos|x (GE Sensing & Inspection Technologies GmbH). For reconstruction, a ring artifact correction, an autoscan optimization and a beam hardening correction were performed. The CT volumes were analyzed using Visual Studio Max 2.2 software (Volume Graphics GmbH, Heidelberg, Germany) and also with a Matlab program (courtesy of B. Cordonnier). For our case, the error of this method essentially depends on the threshold (or segmentation) value used to define the boundary between chromite and silicate minerals. Trial runs with a series of different segmentation values using both processing methods yield deviations in the result of $\pm$2 vol. %.

RESULTS

Norites and anorthosites

The dominant rock type through the 264 m drill core is norite (Fig. 2b) with variations to leuconorite, mottled anorthosite and anorthosite. Representative whole-rock

Table 1: Bulk-rock composition of major elements and the normative mineral proportions in representative rock samples from the studied drill core and the parent magma composition calculated based on Barnes *et al.* (2010)

Rock type:	Chromitite		Peg. px.	Mixed layer	Pyroxenite				Oliv. px.	Mott. an[1]	Nor[1]	Parent magma[2]	Chromite
Depth:	UG2 236·51	UG3 229·27	237·85	236·88	238·82	233·22	226·86	222·54	225·08	220·04	245·80	B1–B2 60:40	236·62
Major elements (wt %)[3]													
SiO_2	8·41	15·1	52·8	34·4	53·8	53·4	52·4	53·5	42·0	48·7	50·6	53·8	0·09
TiO_2	0·71	0·62	0·16	0·40	0·21	0·16	0·19	0·22	0·14	0·05	0·13	0·51	0·75
Al_2O_3	18·0	18·5	7·18	9·91	5·59	6·67	7·12	4·85	4·65	30·4	23·5	13·4	18·8
FeO^{total}	23·8	20·3	9·81	15·8	10·4	9·58	10·2	11·7	13·0	1·11	3·79	10·2	27·7
FeO^{rec}	20·0	17·0		14·7									22·9
$Fe_2O_3^{rec}$	4·18	3·60		1·30									5·34
MnO	0·16	0·15	0·19	0·16	0·21	0·21	0·20	0·24	0·17	0·02	0·07	0·18	0·09
MgO	10·2	9·76	23·1	20·5	23·9	22·1	21·5	23·8	27·3	1·15	6·78	9·87	8·18
CaO	1·85	3·27	4·24	2·01	4·00	6·18	5·95	3·78	4·16	15·3	12·3	8·18	0·03
Na_2O	n.d.	0·02	0·58	n.d.	0·44	0·56	0·57	0·47	0·34	2·34	1·88	1·75	0·01
K_2O	0·15	0·16	0·16	0·68	0·11	0·05	0·06	0·09	0·13	0·14	0·17	0·69	0·02
Cr_2O_3	34·8	30·0	1·15	10·9	0·40	0·29	1·02	0·40	0·34	0·01	0·14	n.r.	43·40
NiO	0·17	0·12	0·09	0·20	0·08	0·07	0·10	0·07	0·19	0·00	0·02	n.r.	n.d.
LOI	–1·28	–1·29	0·17	1·73	–0·07	0·09	–0·01	–0·02	6·49	0·54	0·32	0·29	n.d.
Total	97·70	97·39	99·72	96·77	99·11	99·35	99·35	99·13	98·86	99·78	99·70	98·91	99·08
Mg#	0·43	0·46	0·81	0·70	0·80	0·80	0·79	0·78	0·79	0·65	0·72	0·61	0·34
$Mg^{\#rec}$	0·47	0·51		0·71									0·39
Normative mineral proportions (wt %)													
felds	16·2	24·9	21·3	18·9	17·2	20·8	21·0	15·3	15·3	93·3	74·1		
opx	0·00	4·25	70·3	45·1	75·3	64·7	65·2	77·3	24·7	3·30	20·6		
cpx	0·00	0·00	4·65	0·00	5·97	12·2	11·0	6·35	8·95	3·25	4·56		
oliv	0·00	0·00	0·73	0·00	0·00	1·19	0·00	0·14	49·8	0·00	0·00		
chr*	83·8	70·8	3·01	36·0	1·51	1·11	2·80	0·92	1·20	0·17	0·71		
Total	100	100	100	100	100	100	100	100	100	100	100		

Peg. px., pegmatoid pyroxenite; Oliv. px., olivine pyroxenite; Mott. an., mottled anorthosite; Nor., norite; felds, total feldspars; opx, orthopyroxene; cpx, clinopyroxene; oliv, olivine; chr*, chromite solid solution; n.d., not determined; n.r., not reported. FeO^{rec} and $Fe_2O_3^{rec}$ are FeO and Fe_2O_3 recalculated from chromite stoichiometry. Mg# and $Mg^{\#rec}$ are calculated based on FeO^{total} and FeO^{rec}, respectively.
[1]Anorthosites and norites are not included in the studied profile but are given here for comparison.
[2]Parent magma composition calculated based on Barnes *et al.* (2010), who suggested a 60:40 mixture of B1 and B2 magmas as the parent of the Upper Critical Zone.
[3]Determined by XRF.

major and trace element compositions of these rock types are reported in Tables 1 and 2, respectively (the complete dataset, including measurement errors and detection limits, is provided in Supplementary Data Electronic Appendix 1).

Anorthosites are distinguished by their high Al_2O_3 (29–30 wt %) and low MgO and FeO (1–1·6 wt %) contents, and have almost the same composition throughout the entire drill core. They have normative plagioclase contents of 91–94% with a normative X_{An} of 0·76–0·78. Normative opx and cpx amount to 2–4% and 3–5%, respectively. Norites show more variation in MgO (6–16 wt %), FeO (4–7 wt %) and Al_2O_3 (14–23 wt %) content but have similar SiO_2 contents (51–52 wt %). Normative opx varies accordingly from 22 to 50%, normative plagioclase is 45–74%, and normative X_{An} 0·76–0·77. The norites have mostly no cpx.

UG2–UG3 section: major elements and normative mineral contents

Whole-rock major and trace element compositions of representative rock types are given in Tables 1 and 2 (see also Supplementary Data Electronic Appendix 1). Variations in selected major elements throughout the stratigraphic section are shown in Fig. 5.

Pyroxenites and harzburgites

There is little systematic variation in most of the pyroxenites (hereafter termed 'common') except for the mixed layer and pegmatoid in the footwall of UG2 and for the olivine-rich pyroxenites and harzburgites in the hanging wall of UG3a and UG3b. In the common pyroxenite layers, which have a combined thickness of 18 m, the amount of SiO_2 varies between 52 and 55 wt %, with an average of 53 wt %, except for two pyroxenite samples directly above UG3. The latter contain higher amounts of chromite and have SiO_2 contents of 48 and 50·6 wt % (Fig. 5). Similar to SiO_2, FeO, MgO, and CaO vary within restricted ranges of 9–11 wt %, 21–26 wt %, and 4–7 wt %, respectively. Al_2O_3 and Na_2O vary from 2 to 8 wt % and from 0·02 to 0·9 wt %, respectively, and can be directly correlated with the amount of plagioclase.

The olivine pyroxenites and harzburgites in the hanging wall of UG3a + b have the lowest SiO_2 contents, down to 41·6 wt %, but in terms of the other major oxides they are similar to the olivine-poor or olivine-

Table 2: Bulk-rock composition of trace elements in representative rock samples from the studied drill core and the parent magma composition calculated based on Barnes *et al.* (2010)

Rock type:	Chromitite		Peg. px.	Mixed layer	Pyroxenite				Oliv. px.	Mott. an.[1]	Nor.[1]	Parent magma[2]
Depth:	UG2 236·51	UG3 229·27	237·85	236·88	238·82	233·22	226·86	222·54	225·08	220·04	245·80	B1–B2 (60:40)
Trace elements (mg g^{-1})[3]												
P	286	810	53·3	200	38·2	36·6	286	362	11·4	38·0	32·1	489
Sc	7·29	13·0	25·2	10·4	27·3	30·4	29·6	32·0	18·6	2·57	9·85	31·0
V	1239	1957	144	404	106	152	162	132	74·8	12·4	54·1	194
Cr	185454	245983	8073	51907	2582	1876	6748	2481	2161	77·5	906	659
Co	197	271	95·7	140	83·3	83·0	82·1	88·4	169	6·70	28·1	56·6
Ni	915	1069	725	1152	578	472	734	521	1357	30·2	143	213
Cu	24·1	8·76	7·28	34·6	18·7	16·9	14·7	31·7	88·8	7·22	4·45	61·0
Zn	408	532	73·5	178	48·2	51·2	63·0	64·3	56·5	8·05	19·7	84·1
Ga	38·5	52·9	7·07	14·7	5·23	4·81	4·69	4·96	4·28	14·4	13·2	16·5
Ge	n.d.	n.d.	2·12	n.d.	2·23	n.d.	n.d.	4·67	5·06	n.d.	n.d.	n.r.
Rb	2·80	5·57	5·37	16·8	2·08	0·57	0·85	2·74	2·84	1·20	2·35	25·5
Sr	44·4	123	115	53·6	86·0	88·6	105	72·3	75·4	458	357	258
Y	1·49	5·08	3·38	1·73	5·30	3·51	5·21	6·71	4·62	0·86	3·05	14·8
Zr	16·1	22·4	12·4	8·62	11·0	6·06	8·15	14·6	14·3	4·17	13·7	67·9
Nb	1·00	n.d.	0·50	1·34	0·51	n.d.	n.d.	0·46	0·56	0·30	0·60	4·04
Mo	n.d.	n.d.	0·78	2·94	0·72	0·49	1·13	n.d.	0·56	n.d.	1·04	n.r.
Sn	n.d.	16·43	2·10	n.d.	1·45	n.d.	n.d.	4·12	3·43	3·71	n.d.	n.r.
Cs	n.d.	n.d.	0·33	0·44	0·11	n.d.	0·14	0·15	0·49	n.d.	0·12	1·66
Ba	40·2	95·9	54·2	167	37·2	28·2	40·7	40·5	39·8	72·4	96·0	295
La	1·63	5·23	2·85	1·37	3·14	1·22	3·95	4·64	2·33	2·18	4·06	16·8
Ce	3·08	9·94	5·55	2·09	6·44	2·86	8·22	8·61	5·02	3·71	7·89	33·6
Pr	0·40	1·03	0·54	0·43	0·77	0·25	1·02	1·09	0·66	0·37	0·84	4·11
Nd	1·60	5·08	2·09	n.d.	2·95	1·78	4·13	4·61	2·88	1·37	3·19	16·2
Sm	n.d.	n.d.	0·55	n.d.	0·59	0·31	0·98	0·90	1·02	n.d.	0·71	3·18
Eu	0·47	n.d.	0·24	n.d.	0·31	0·17	0·33	0·23	0·32	0·38	0·47	1·02
Gd	n.d.	n.d.	0·38	n.d.	0·81	0·34	0·76	1·44	0·78	n.d.	0·74	2·88
Tb	n.d.	n.d.	0·07	n.d.	0·15	0·11	0·22	0·12	0·12	n.d.	0·11	0·42
Dy	n.d.	1·66	0·47	n.d.	1·08	0·56	0·71	1·23	0·19	0·50	0·79	2·42
Ho	0·23	n.d.	0·11	n.d.	0·22	0·15	0·31	0·18	0·22	n.d.	0·11	0·49
Er	n.d.	n.d.	0·47	n.d.	0·60	0·42	0·79	0·88	0·69	n.d.	n.d.	1·35
Tm	n.d.	n.d.	0·05	n.d.	0·10	0·07	n.d.	0·16	0·04	n.d.	0·06	0·20
Yb	n.d.	n.d.	0·40	2·77	1·01	0·54	n.d.	1·44	0·56	n.d.	n.d.	1·35
Lu	n.d.	n.d.	0·08	n.d.	0·12	n.d.	0·20	0·14	n.d.	n.d.	0·08	0·21
Hf	1·40	n.d.	0·40	n.d.	0·36	0·35	n.d.	0·67	0·35	n.d.	0·35	1·68
Ta	n.d.	n.d.	0·06	n.d.	n.d.	0·10	n.d.	0·07	n.d.	0·07	n.d.	0·42
Pb	n.d.	n.d.	1·46	1·86	1·25	0·18	0·40	0·84	2·23	0·80	0·61	10·0
Th	n.d.	0·79	0·61	n.d.	0·20	n.d.	0·39	0·63	0·35	0·20	0·50	2·35
U	n.d.	n.d.	0·23	0·59	0·09	n.d.	0·13	n.d.	0·12	n.d.	n.d.	0·68
K	1068	323	1333	4062	891	n.d.	491	707	1082	1072	1378	5711

Peg. px., pegmatoid pyroxenite; Oliv. px., olivine pyroxenite; Mott. an., mottled anorthosite; Nor., norite; n.d., not determined; n.r., not reported.
[1]Anorthosites and norites are not included in the studied profile but are given here for comparison.
[2]Parent magma composition calculated based on Barnes *et al.* (2010), who suggested a 60:40 mixture of B1 and B2 magmas as the parent to the Upper Critical Zone.
[3]Determined by LA-ICP-MS.

absent common pyroxenites. Bulk Mg-numbers [Mg/(Mg + Fe^{total})] for all the pyroxenites and the harzburgites vary little, between 0·79 and 0·81 (Fig. 6).

Distinct variations in Na_2O and Al_2O_3 bulk-rock contents occur in the pegmatoid footwall pyroxenites of UG2 and UG3. However, with a grain size of up to 2–3 cm in a core of 2 inch diameter, the representativeness of the bulk-rock analyses cannot be guaranteed. The abruptly higher Na_2O and Al_2O_3 contents immediately above UG2 (Fig. 5) correspond to the thin leuconorite to anorthosite layer described above (Figs 2c and 4a).

Variations in normative mineralogy based on the CIPW norm are shown in Fig. 7. The normative modes correspond well to observations in thin section. Opx is the dominant mineral phase, forming on average 75 wt % of the common pyroxenites. Plagioclase, the second most dominant phase, is typically 8–24%, but reaches 77% in the leuconorite to anorthositic sample in the hanging wall of UG2 (profile Fig. 6).

Normative anorthite contents (X_{An}) range between 0·60 and 0·82 in the common pyroxenites (Fig. 6). Normative cpx constitutes on average 9 wt % of the common pyroxenite layers, but varies unsystematically throughout the profile from 5·0 to 15%. The appearance of up to 58% normative olivine in the olivine pyroxenites to harzburgites in the hanging wall of UG3b is consistent with thin-section observations. Based on their normative mineral contents the cumulates are plotted

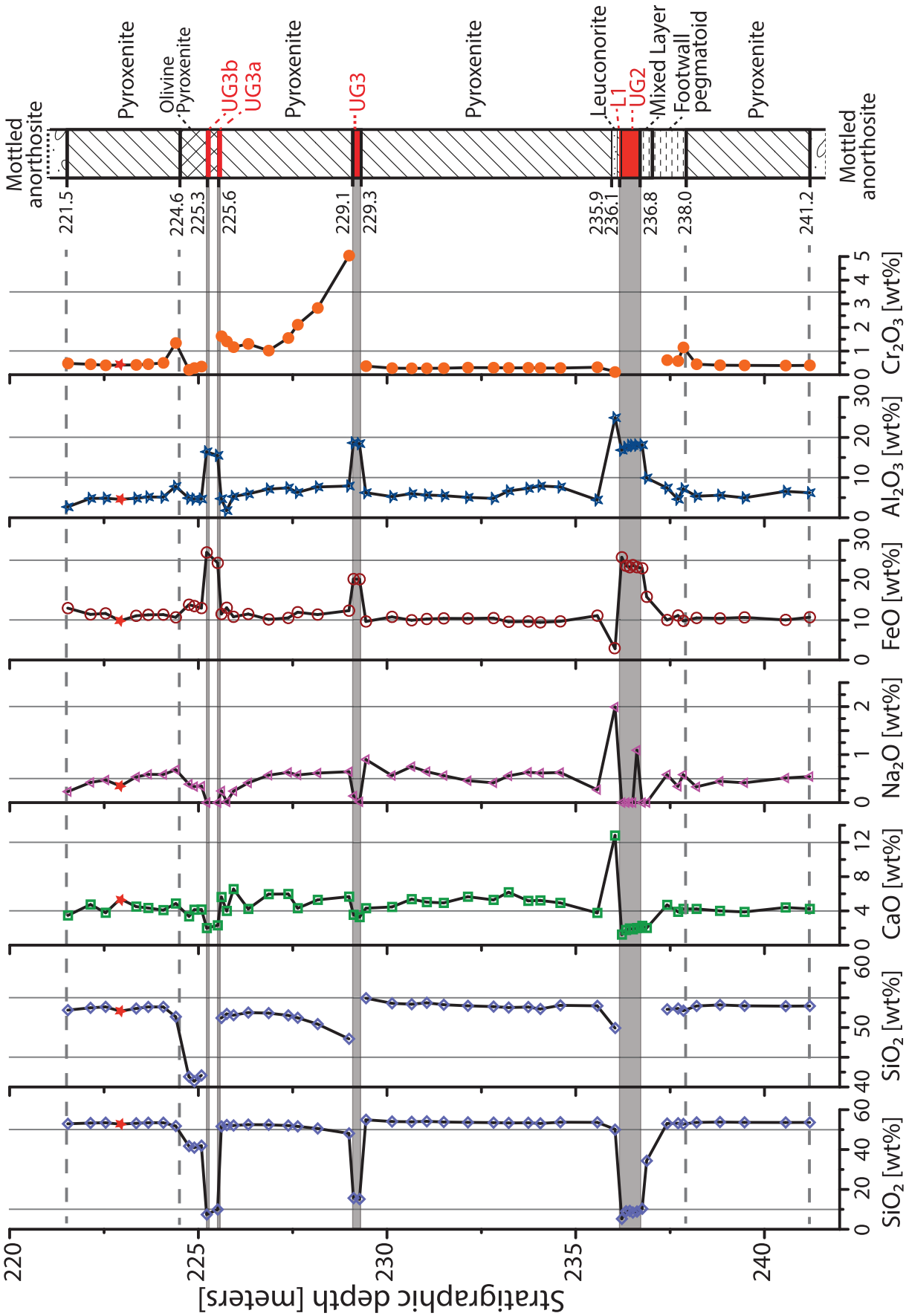

Fig. 5. Variations in bulk-rock concentrations of selected major elements in the studied section. The Cr content in the chromitites is off-scale. Location of the altered sample (MP-222.93) is shown with a red star.

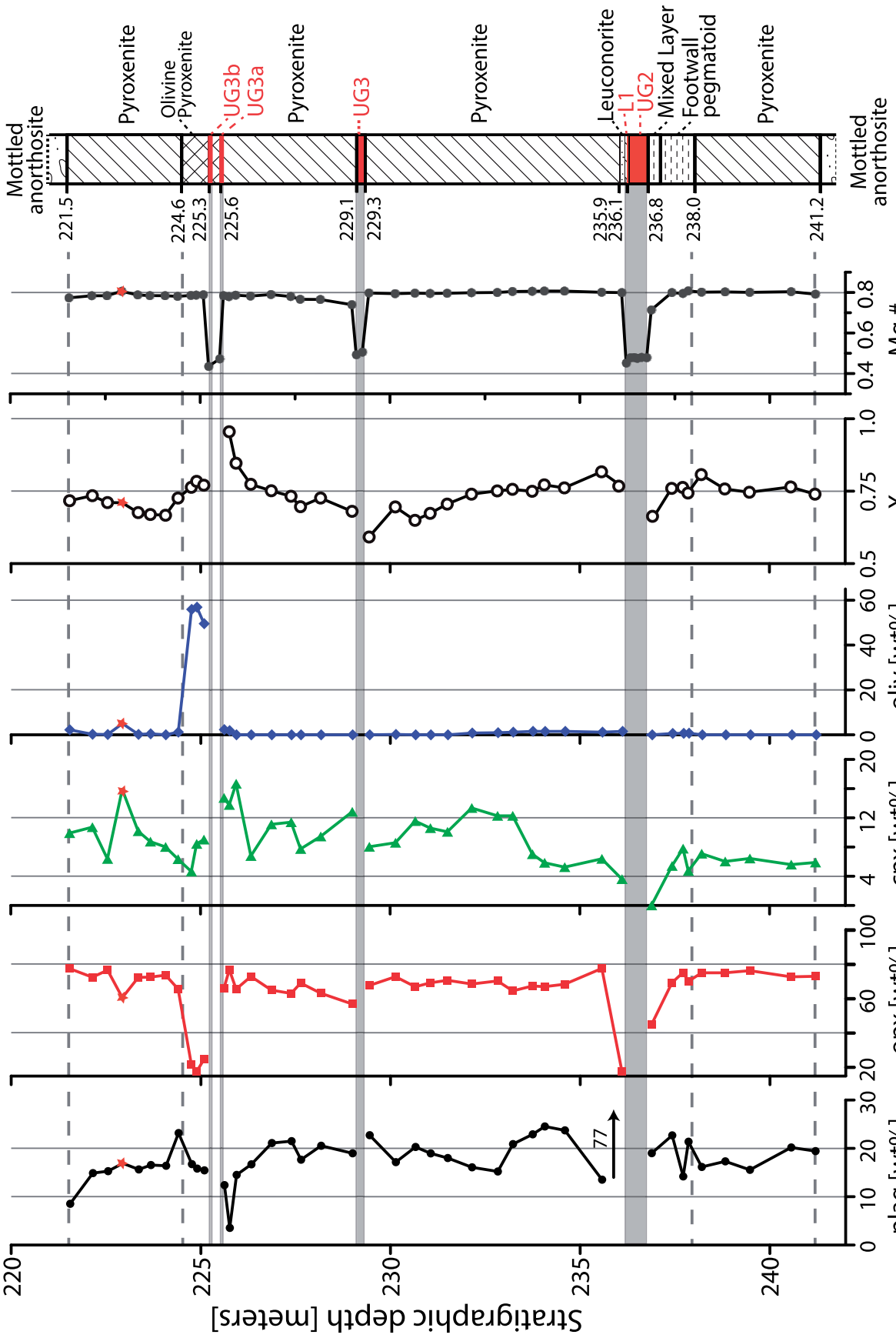

Fig. 6. Variations in normative minerals through the studied section. Anorthite content of plagioclase (X_{An}) is calculated based on the CIPW norm. Mg-number in silicate rocks is calculated using the FeO^{total} of bulk-rock analyses and in chromitites it is calculated based on Fe^{2+} recalculated from chromite stoichiometry. Position of the altered sample (MP-222.93) is marked with a red star.

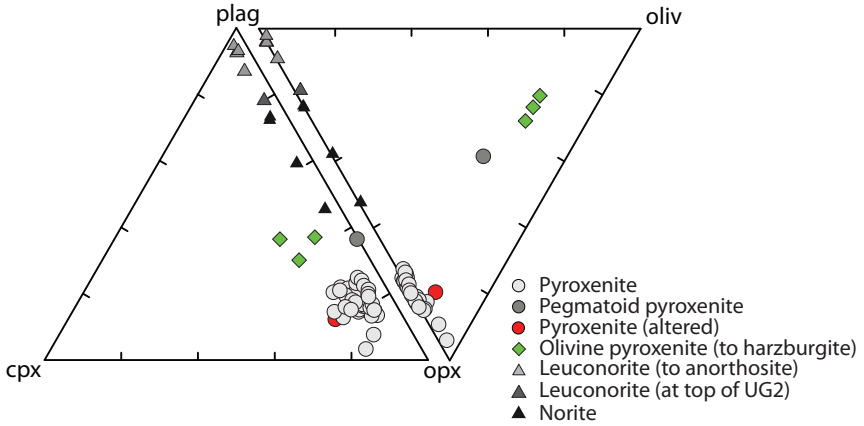

Fig. 7. Ternary plots of plagioclase–opx–cpx and plagioclase–olivine–opx based on the CIPW norm of the bulk-rock compositions.

in the plag–opx–cpx and plag–opx–olivine ternaries (Fig. 7). The normative mineral mode of the pegmatoid pyroxenite of the UG2 footwall is shifted towards the olivine-rich corner, an artifact related to the abundance of phlogopite and amphibole, both hydrous low-Si minerals not represented in the CIPW norm calculation.

Chromitites

SiO_2 contents in the chromitites are 5–16% and Cr_2O_3 ranges from 29 to 35 wt %. Bulk-rock Mg-numbers have been calculated based on Fe^{total} (as in all other rock types) and are 0·40–0·46. As considerable amounts of Fe are in the trivalent state (ferric) in the chromite, we have also calculated Mg-number$^{rec} = Mg/(Mg + Fe^{2+})$ based on Fe^{2+} recalculated from chromite stoichiometry. These values vary between 0·44 and 0·51, increasing the Mg-number based on Fe^{total} by 0·05. The Al, Fe and Mg contents are much higher than in the pyroxenites, whereas CaO and Na_2O contents are much lower (Table 1 and Fig. 5). As discussed under 'Methods', a somewhat modified mineral norm needs to be employed. This normalization scheme results in 70–90 wt % chromite (total spinel group components), 0–4 wt % opx, and 10–28 wt % feldspar with normative X_{An} of 0·56–0·76. The normative opx content is lower than observed, a consequence of accommodating all K, Na, and Ca in normative feldspar whereas in the actual rocks the low-Si minerals phlogopite and amphibole amount to several per cent of the total rock (i.e. several tens of per cent of the silicate fraction).

UG2–UG3 section: trace element concentrations

To illustrate the variations in trace element contents throughout the profile, the concentrations of selected incompatible trace elements (all determined by LA-ICP-MS) are plotted versus stratigraphic height (Fig. 8). Variation patterns in whole-rock K, Rb, Ba and Cs concentrations are almost identical, Ba showing slightly more variation across the profile. These larger variations in Ba may be due to its higher partition coefficient in plagioclase when compared with other generally incompatible elements (Bédard, 2006; Frei *et al.*, 2009). The highest concentrations of incompatible elements are observed in the pegmatoid pyroxenites in the footwall of the UG2 and UG3 chromitite layers. Unintentionally we also sampled a macroscopically invisible altered zone in the hanging-wall pyroxenite of UG3b. In thin section this sample contains abundant greenschist-facies minerals such as chlorite, tremolite, actinolite and saussuritized plagioclase (Fig. 4d). This zone is heavily enriched in fluid-mobile trace elements, probably related to infiltration of post-magmatic fluids.

Other incompatible trace elements include P, Th and Zr, which are also illustrated in Fig. 8. Uranium is mostly below or close to the detection limit and hence is not useful for the purpose of this study. In most studies P is considered as a perfectly incompatible element in ultramafic cumulates containing pyroxene, plagioclase and olivine (e.g. Cawthorn & Walsh, 1988; Tegner *et al.*, 2009). However in our section, strong variations in P are common and local enrichments to concentrations close to or higher than the estimated parent magma composition are observed. In the pyroxenites, higher P concentrations correlate moderately well with higher rare earth element (REE) concentrations. However, REE melt/apatite partition coefficients are only 2–4 for depolymerized melts (Prowatke & Klemme, 2006), and would not lead to a correlation of REE with apatite accumulation, as long as the amount of apatite permitted by the bulk-rock P concentration is $<$0·2%. UG2 and UG3 have P concentrations that are 3–8 times those of the adjacent pyroxenites and twice those of the proposed parent magma (Table 2); nevertheless, REE concentrations are similar in the pyroxenites and chromitites. Element and phase distribution maps show that in the chromitites apatite clusters in small areas (about 1 cluster per cm^2; see Supplementary Data Electronic Appendix 2), rendering representative image analysis difficult. Nevertheless, the relatively high P concentrations in the chromitites can be attributed to cumulus apatite. In summary, the P variations may be interpreted as a result of apatite beginning to crystallize before melt

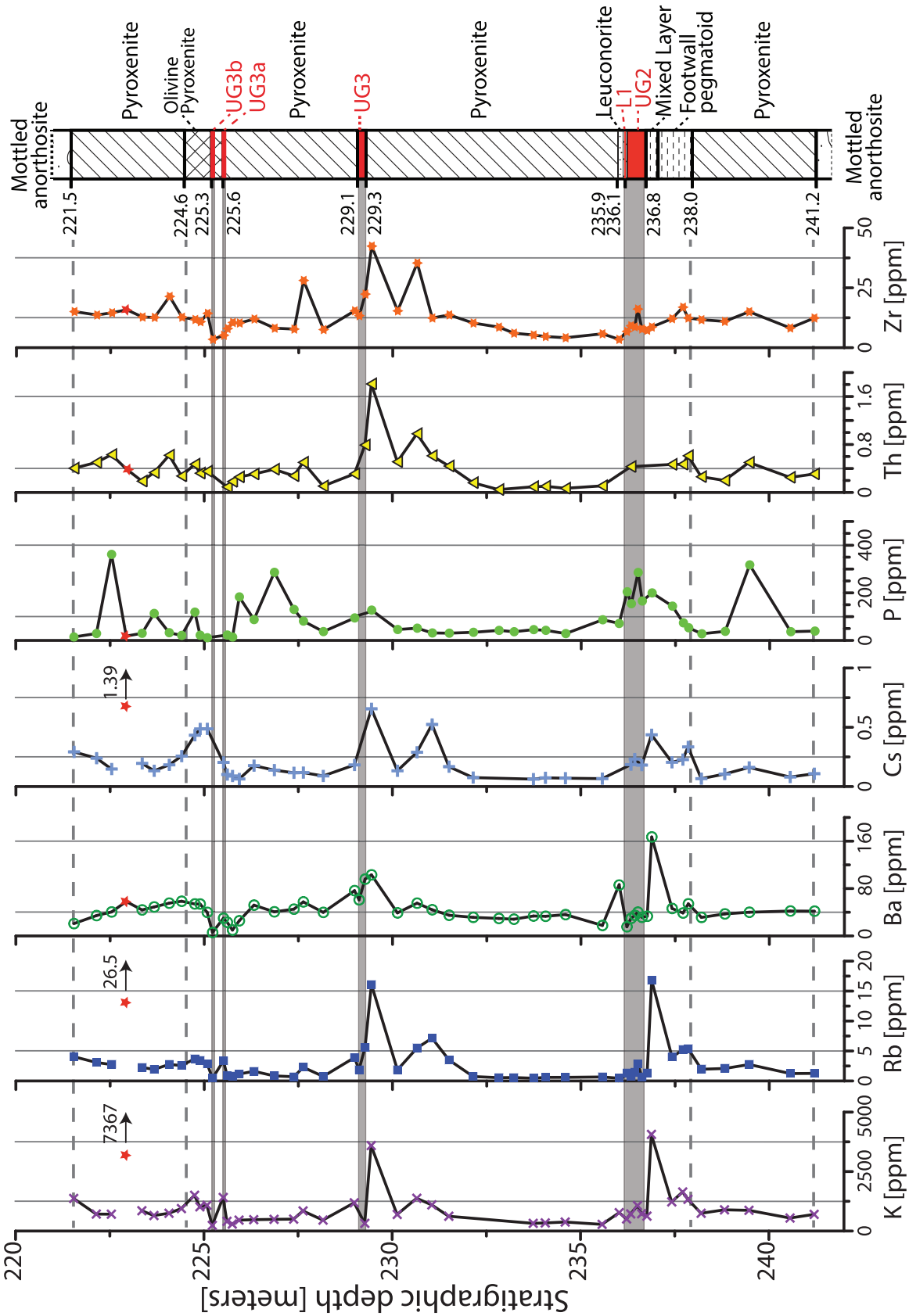

Fig. 8. Variations in bulk-rock concentrations of selected trace elements through the studied section. Arrows and numbers correspond to the trace element concentrations in the enriched sample altered at greenschist facies (MP-222-93); the position of this sample is shown with a red star.

expulsion and compaction stopped, providing an illustration of fractionation during compaction (e.g. Boudreau *et al.*, 1986; Meurer & Meurer, 2006).

Trapped liquid calculations

The aim of this study was to reconstruct the paleoporosity of the cumulate section at the point in time where compaction (and hence interstitial liquid expulsion) stopped. A conventional method for calculating trapped liquid fraction (F_{TL}) is based on comparing the bulk concentration of perfectly incompatible elements in the cumulate rock with the concentration of those elements in the magma from which the cumulate crystallized (e.g. Henderson, 1970; Cawthorn & Walsh, 1988). The trapped liquid fraction (F_{TL}) is then obtained from

$$F_{TL} = C_i^{cum}/C_i^{liq}$$

where C_i^{cum} is the concentration of the incompatible element i in the cumulate bulk-rock and C_i^{liq} is the concentration of the same element in the parent liquid. A perfectly incompatible element is exclusively present in the melt interstitial to the cumulate minerals and therefore its concentration is representative for the liquid fraction ultimately crystallized in a given rock volume. Nevertheless, some caution is appropriate, as fractionation during compaction and interstitial liquid expulsion is possible. Furthermore, the composition of the parent magma during cumulate formation may change (e.g. Mathez *et al.*, 1997; Tegner *et al.*, 2009). In our studied section, the absence of variations in Mg-numbers indicates little evolution of the parent liquid (Fig. 6). Because P is compromised we rely on Cs, Rb, K, Ba, Zr and Th concentrations, which all show relatively constant ratios, indicating negligible fractionation and closed-system crystallization of the residual interstitial liquid.

The next complexity for calculating trapped liquid contents arises from approximating the parent magma composition of the Rustenburg Layered Suite in the Bushveld Complex (Cawthorn, 2007; Barnes *et al.*, 2010). Barnes *et al.* (2010) have suggested that a 60:40 mixture of B1 and B2 magmas (Tables 1 and 2) has a composition that would produce the observed crystallization sequence of the Upper Critical Zone. This composition has therefore been used to estimate the trapped liquid content of the studied section that is part of C_UZ.

The choice of element for calculating the trapped liquid content is based on the degree of its (in)compatibility in the cumulus minerals, which are olivine, opx and chromite. Between opx and anhydrous silicate melt (Frei *et al.*, 2009) elements such as Ba, Cs, K, Rb and Th have partition coefficients $< 0{\cdot}01$ and Zr $< 0{\cdot}1$. These elements also have partition coefficients $< 0{\cdot}01$ in olivine (Philpotts & Schnetzler, 1970; Villemant, 1988; Beattie, 1993, 1994). Consequently, the fractions of trapped liquid based on each of these elements should give similar values (see below). Calculated trapped liquid fractions from the K, Rb, Ba, Cs, Th and Zr contents of the bulk-rocks and the B1–B2 mixture are shown in Fig. 9.

Excluding the footwall pegmatoid pyroxenites, the calculated trapped liquid weight fractions are ~0·02–0·28 based on the Rb bulk-rock content, 0·02–0·34 based on Th, 0·02–0·33 based on Ba, 0·04–0·32 based on Cs, 0·05–0·41 based on Zr and 0·04–0·29 based on K. These values are in the same range as trapped melt contents (0·05–0·30) in the Critical Zone of the Bushveld Complex reported by Maier *et al.* (2013) based on the whole-rock Zr content with respect to the B1 magma. Nevertheless, Veksler *et al.* (2014) have noted that, for calculating trapped liquid contents, Zr should be used with caution and needs to be compared with results from other incompatible elements.

Trapped liquid fractions in the pyroxenites and harzburgites

The average trapped liquid fraction has been calculated based on the concentrations of K, Rb, Ba, Cs, Th and Zr (Supplementary Data Electronic Appendix 3) and the results are compared in Fig. 9. Based on these calculations, the main units in the profile have the following trapped liquid weight fractions: the lower 3 m of the UG2 footwall pyroxenite have a relatively constant trapped liquid fraction of 0·12(2), followed by an increase to 0·19(3) in the lower part of the UG2 footwall pegmatoid. The trapped liquid weight fraction is then 0·05–0·23 in the UG2 hanging-wall pyroxenites, almost continuously increasing with stratigraphic height. For the lower 5 m of this pyroxenite the average liquid fraction is 0·09(2). The harzburgites, olivine pyroxenites and pyroxenites in the hanging wall of UG3b have trapped liquid fractions between 0·13 and 0·20 [with an average of 0·17(2)] without much systematic variation.

Comparison between the average liquid fraction and values calculated from single trace elements show that the liquid fractions calculated from K are closest to the mean, whereas those from Rb, Cs and Ba yield mostly lower liquid fractions and Zr yields systematically higher values. A systematic deviation from the mean, as is the case for the liquid fraction calculated from Zr, could be taken as an indication that Zr concentrations in the calculated parent magma are underestimated. However, it is beyond the scope of this study to modify the proposed parent magma composition.

Trapped liquid fractions in the chromitites

The calculation of trapped liquid fractions in the chromitite layers (UG2, UG3 and their leaders) is based on four methods: (1) the incompatible trace element content method as described above; (2) the SiO_2 content of the chromitite cumulates compared with the SiO_2 content of the parent magma (Fig. 9); (3) for the sample in which the chromite composition was measured, the Cr content in the bulk-rock compared with the Cr content of

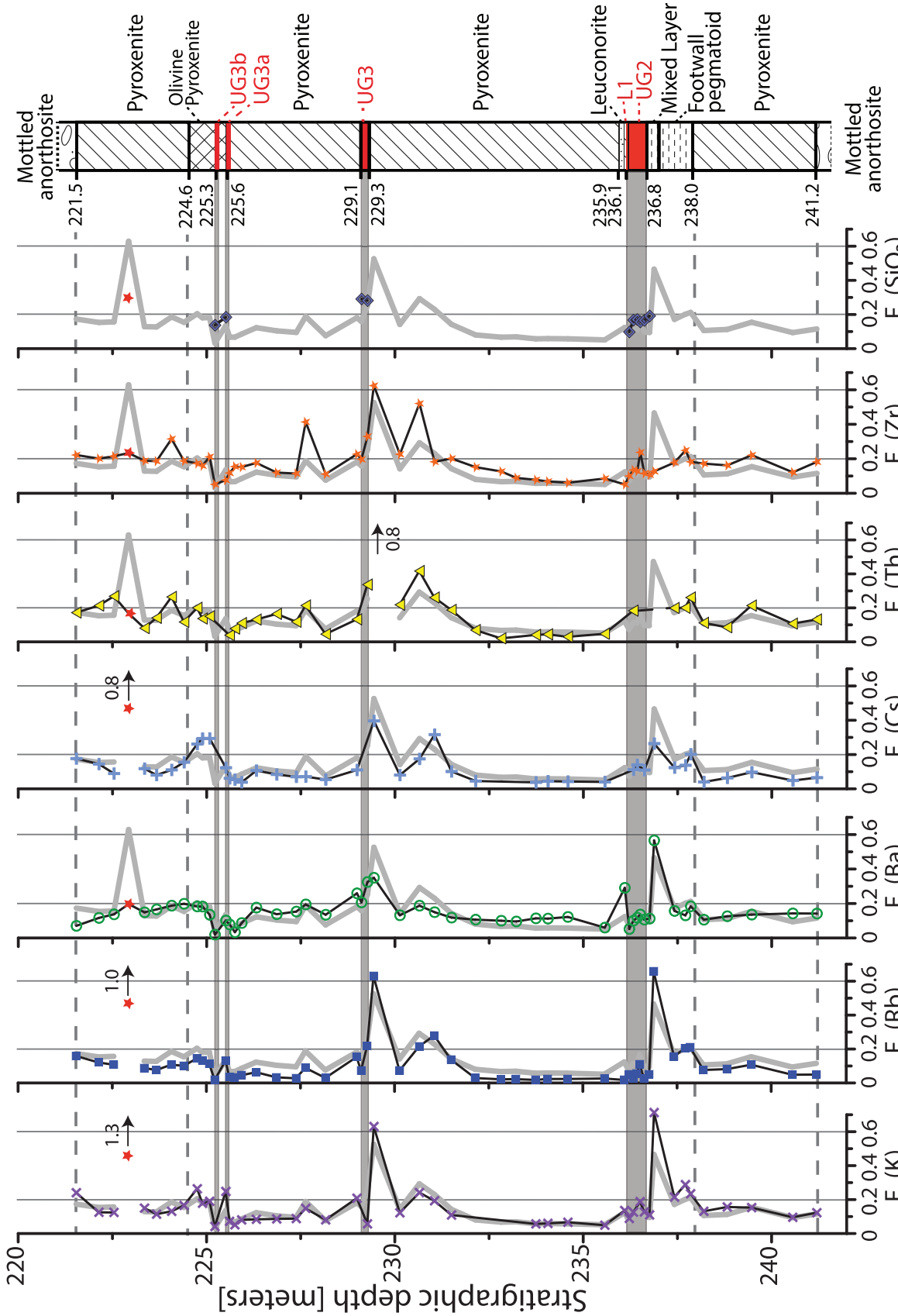

Fig. 9. Trapped liquid fractions (F_{TL}) calculated based on the weight fraction of different trace elements in the bulk-rock (colored symbols) relative to a B1–B2 mixture (60:40) as the parent magma to the Upper Critical Zone (Barnes *et al.*, 2010). An average trapped liquid content from these trace elements has been calculated and is shown as the light gray line in the profile for each element. In chromitite samples, the fraction of trapped liquid is calculated based on the bulk-rock SiO_2 content. Arrows and numbers correspond to extreme trapped liquid fractions calculated for some pegmatoids and the altered sample (red star).

the chromite; (4) 3D X-ray CT for two chromitite samples (Supplementary Data Electronic Appendix 3). The use of the bulk-rock SiO_2 content of the chromitites to calculate trapped liquid weight fractions is based on the fact that no SiO_2 is incorporated into chromite, hence in a system where no fractionation of silicates occurs

$$F_{TL} = C^{cum}_{SiO_2} / C^{liq}_{SiO_2}.$$

Similarly, the liquid weight fraction based on Cr concentrations can be calculated by simple mass balance from

$$1 - F_{TL} = C^{cum}_{Cr_2O_3} / C^{chromite}_{Cr_2O_3}$$

neglecting the small Cr concentration in the parent liquid (<0·1 wt %; Tables 1 and 2). The average of calculated liquid weight fractions based on incompatible elements is 0·07–0·17 in UG2, 0·16–0·25 in UG3, 0·14 in UG3a and 0·03 in UG3b. Based on SiO_2, trapped liquid fractions result as 0·10–0·19 in UG2, 0·28 in UG3, 0·18 in UG3a and 0·14 for UG3b (single sample values are given in Supplementary Data Electronic Appendix 3).

Silicate melt contents calculated from trace element, SiO_2 or Cr concentrations are weight fractions, which need to be converted to volume fractions for porosity modeling. For this, we assume an average density for the silicate cumulate minerals (opx, cpx and olivine) of 3300 kg m^{-3} (Jordan, 1979), a melt density of 2720 kg m^{-3} (Stolper & Walker, 1980) and a chromite density of 4600 kg m^{-3} (Deer *et al.*, 1992). Volume fractions are shown in Fig. 10. The samples in which the volume fractions of chromite versus total silicate minerals were directly measured by X-ray tomography resulted in 32(2) vol. % silicates for MP-236·33 (UG2) and in 43(2) vol. % silicates for MP-229·11 (UG3). In the UG2 sample, the 32(2) vol. % measured from X-ray tomography may be compared with 32(3) vol. % silicates calculated from Cr contents, 25(8) vol. % silicates calculated from SiO_2 contents and 15·4(6) vol. % silicates calculated from trace elements. For the UG3 sample the 43(2) vol. % obtained from X-ray tomography may be compared with 41(5) vol. % silicates from the SiO_2 content and 24·2(1·1) vol. % silicates calculated from trace elements. The reason for these differences is discussed below.

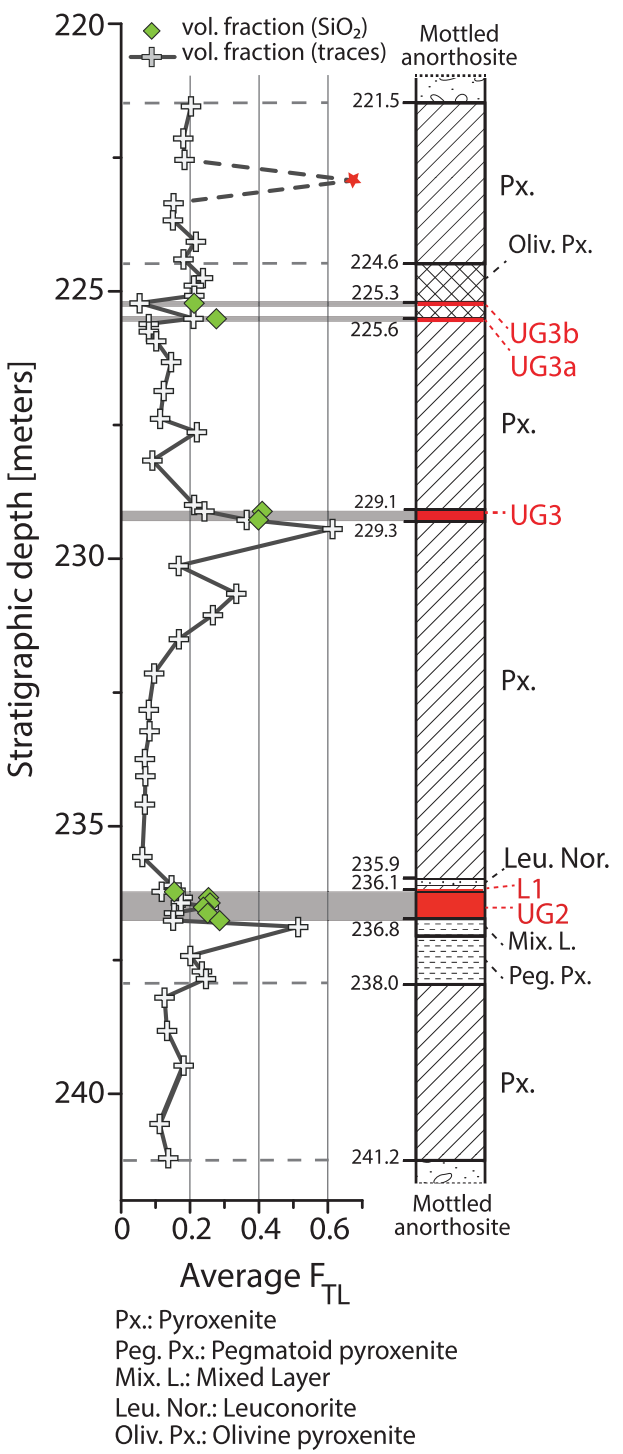

Fig. 10. Average volume fraction of trapped liquid (F_{TL}) calculated based on different trace elements (dark grey line and crosses) compared with the average volume fractions calculated based on bulk-rock SiO_2 content (green diamonds) in the chromitite samples. Position of the altered sample (MP-222·93) is shown with a red star.

Footwall pegmatoids

Within the studied cumulate section three samples have high apparent calculated trapped liquid contents. Sample MP-236·88 corresponds to the pegmatoid mixed layer in the footwall of UG2 (average $F_{TL} = 0·47$). Two other samples, MP-229·44 and MP-230·65, correspond to the coarse-grained plagioclase pyroxenites in the footwall of the UG3 chromitite layer (Fig. 9) and have calculated F_{TL} of up to 0·57. These samples are also enriched in interstitial phases such as phlogopite and amphibole, which incorporate the otherwise most suitable trace elements K, Rb, Ba, Cs, Zr and, to a lesser extent, Th. An enrichment in incompatible trace elements in pegmatitic rocks has been reported in similar rocks from the footwall of the Merensky Reef in the Bushveld Complex (e.g. Veksler *et al.*, 2014). These pegmatoid pyroxenites are interpreted to be derived from residual melts rising through the cumulate pile and

collecting below an apparent permeability barrier (i.e. the chromitites; Mathez & Mey, 2005).

Low-temperature alteration

Another sample with a high apparent amount of calculated trapped liquid is MP-222·93 (Fig. 9). In thin section (Fig. 4d) this sample is altered to a greenschist-facies mineralogy, including muscovite, tremolite, actinolite and saussuritized plagioclase, leading to high K, Rb and Cs concentrations. The high calculated F_{TL} is hence an artifact of this secondary alteration.

DISCUSSION

Incompatible element enriched zones

Pegmatoid rocks at the base of dense chromitite layers (e.g. UG2) in the Bushveld Complex are common features (e.g. Viljoen & Scoon, 1985; Viljoen *et al.*, 1986; Barnes & Campbell, 1988; Cawthorn & Barry, 1992; Mathez & Mey, 2005; Mondal & Mathez, 2007; Maier & Barnes, 2008; Maier *et al.*, 2013). Detailed studies of textures, modes and composition of minerals in pegmatoid rocks in LMIs in general (e.g. Vermaak, 1976; Ballhaus & Stumpfl, 1985; Naldrett *et al.*, 1986; Nicholson & Mathez, 1991; Boorman *et al.*, 2003), and in footwall pyroxenites of the UG2 chromitite in particular (Mathez & Mey, 2005; Mondal & Mathez, 2007), have revealed high abundances of interstitial halogen-rich phlogopite and more sodic and potassium-rich feldspar. These are interpreted as the result of two main processes: the first is *in situ* crystallization of high amounts of interstitial melt owing to fractional crystallization; the second is recrystallization and metasomatism under the influence of a hydrous melt that infiltrated upwards during compaction. In either case the presence of a relatively impermeable layer of chromitite is thought to prevent the expelled interstitial melt escaping from the lower layers. The cumulate + trapped liquid concept is not easily applicable to the pegmatoid rocks because (1) local fractionation or accumulation of phlogopite, biotite, or accessory minerals may occur and modify the trace element contents used to calculate trapped liquid fractions, and (2) evidence for fluid saturation (Boudreau *et al.*, 1986; Willmore *et al.*, 2000) indicates possible fractionation of highly fluid-soluble elements such as K, Rb, and Cs. The relatively high concentrations of incompatible trace elements support an origin of the pegmatoids from more fractionated melts; nevertheless, the trapped liquid fractions calculated for the pegmatoids should probably not be taken at face value.

In contrast to the model of accumulation of late interstitial melts, Cawthorn & Boerst (2006) have argued that if a fluid or residual magma was responsible for the formation of such pegmatoid layers, these should be enriched in incompatible elements. Their whole-rock data for pegmatoids from the base of the Merensky Reef and UG2 at Union Mine (Western Bushveld) are almost identical to those for the pyroxenites and lack enrichment in incompatible trace elements. Based on these data Cawthorn & Boerst (2006) constructed a model that explains the coarse-grained pegmatoids as the products of recrystallization owing to reheating by intruding new, hot, primitive magma, the latter ultimately leading to the chromitite and pyroxenite layer formation above the pegmatoids (Cawthorn & Barry, 1992; Cawthorn & Boerst, 2006). Other processes such as an enhanced cooling rate or textural evolution of the crystalline matrix may also cause local increase in the trapped melt content within layered intrusions (Mathez *et al.*, 1997).

In the studied drill core the footwall pegmatoid rocks of the UG2 and UG3 chromitite layers are clearly enriched in incompatible trace elements (Fig. 8), as well as phlogopite and amphibole. These observations would be consistent with the pegmatites representing infiltrations of more fractionated and hence H_2O-rich residual interstitial melt. As we will show below, the compaction process in the underlying layers should be efficient and compaction times short enough to allow the upward movement of interstitial melt. The 2 inch diameter drill core used in this study does not allow identification of the larger scale intrusive situation and renders the study of these coarse rock types difficult. Nevertheless, as observed in many other sections, the footwall pegmatoids are discordant to the pyroxenites. The layer with irregularly distributed abundant chromite just below UG2 is analogous to an often observed chaotic mingling between chromitite and pegmatoid at the base of the chromitites. This appears to form a relatively impermeable barrier above the pegmatoids (Mathez & Mey, 2005).

A critical appraisal of calculated paleo-porosities

In a system in which the melt interstitial to the cumulate minerals conserves its chemistry and simply freezes or crystallizes, such that its bulk-rock chemistry remains unchanged, calculation of trapped liquid fractions from strongly incompatible (or, in the case of Cr, strongly compatible) elements is straightforward. However, there are important caveats, as discussed by Barnes (1986), Mathez *et al.* (1997), Meurer & Boudreau (1998*a*) and Meurer & Meurer (2006), as post-cumulus magmatic processes may complicate the picture.

(1) The principle of compaction is that liquid escapes upwards and consequently, in a given cumulate volume, the liquid may originate from a lower level in the cumulate layer. Within the same cumulate layer this process would not lead to modifications in the melt chemistry, but some liquid may arise from deeper, earlier compacted layers that have cooled more extensively and hence contain a more evolved interstitial liquid. This latter melt would be enriched in incompatible trace elements, such that using the parent liquid composition leads to an overestimation of paleo-porosity

(e.g. Mathez *et al.*, 1997; Meurer & Boudreau, 1998*a*).

(2) The interstitial liquid may not simply freeze isochemically, but may cool and partly crystallize while the melt is still percolating through the cumulate pile.

(2a) Incompatible elements may become enriched in the bulk-rock by crystallization of accessory phases that modify specific trace element concentrations. In our case such fractional crystallization is indicated for apatite, as P concentrations vary widely and sometimes exceed those of the inferred parent liquid; hence trapped liquid fractions calculated from P can be $>100\%$, grossly inconsistent with the results from other incompatible elements. Nevertheless, P has been used in studies of other intrusions with great success [e.g. Tegner *et al.* (2009) for the Skaergaard intrusion, Greenland].

(2b) Cumulus phases may crystallize from the interstitial melt while the interstitial melt remains in equilibrium with the parent magma reservoir and hence is essentially unchanged. Such a case may be best exemplified in the chromitites: while chromite is deposited as a chromitite layer, chromite is probably the only liquidus phase. In a second step opx-dominated cumulates are deposited on top (i.e. the parent magma is saturated in opx). In this case opx might crystallize from the interstitial melt in the chromitite, which may, however, equilibrate with the main magma reservoir, such that enrichment in incompatible elements is avoided. In this case, the post-chromite opx is also a cumulus mineral (but not gravitationally settled). As opx is essentially devoid of incompatible elements, the bulk-rock would have relatively lower incompatible element concentrations than if the melt froze isochemically; hence paleo-porosities for the chromite-only stage would be underestimated.

(3) During crystallization, any magma with an appreciable initial H_2O concentration will result in H_2O-rich or H_2O-saturated final liquid compositions. In Bushveld such H_2O-rich compositions are documented by small fractions of either homogeneously distributed phlogopite and amphibole or by small patches or veinlets enriched in these phases (e.g. Vermaak, 1976; Ballhaus & Stumpfl, 1985; Nicholson & Mathez, 1991; Boorman *et al.*, 2003; Mathez & Mey, 2005). Such samples are petrographically and geochemically easy to identify and cannot be used to infer paleo-porosities.

Process (2b) may explain the difference in the volume fraction of trapped liquid calculated from incompatible trace elements and from Cr and SiO_2 concentrations or X-ray tomography of the chromitites. Average volume fractions in UG2 calculated from incompatible trace elements yield 0·17(6) trapped liquid, but from SiO_2 and Cr contents we calculate a silicate matrix fraction of 0·24(4) and 0·32(4), respectively; the latter is in exact agreement with the tomography result of 0·32(2). The SiO_2 content of Bushveld opx (typically 54 wt %; e.g. Mondal & Mathez, 2007) is similar to that of the parent liquid composition (53·8 wt %; Table 1) and hence SiO_2 concentrations, as well as Cr_2O_3 concentrations, should provide a robust estimate of the silicate fraction in the chromitites, irrespective of post-cumulus opx crystallization. Nevertheless, the silicate fraction in the chromitites does not necessarily correspond to the trapped liquid fraction. The ~7 vol. % of large poikilitic opx overgrowing the chromite corresponds to 25% of the space occupied by the silicate fraction. If during the growth of the poikilitic opx the remaining melt remains unchanged owing to equilibration with the magma reservoir, this would lead to a proportionally lower incompatible trace element concentration and hence the trapped liquid fraction calculated from the chromitites may rather correspond to the trapped liquid fraction after crystallization of the poikilitic opx. For the silicate cumulates there is no independent method of verifying the calculated paleo-porosities and we take the, within error, almost identical liquid fractions calculated from six different trace elements as an indication that the calculated trapped liquid fractions correspond closely to calculated paleo-porosities, albeit with typical errors of 3–6 vol. %.

Evaluation of compaction in the studied profile

To determine the efficiency of compaction, we quantify compaction time scales (Fig. 11) and evaluate whether these are within the characteristic range of cooling times for such a cumulate pile. On the basis of centrifuge experiments, Schmidt *et al.* (2012) and Manoochehri & Schmidt (2014) defined equations and bulk cumulate viscosities that permit quantification of compaction rates for olivine and chromite. These equations allow estimation of the effect of simultaneous compaction of several cumulate layers on porosities. Porosity profiles within such layers can be calculated from

$$\varphi_{(h)} = \left[k_1 \ln\left(\Delta\rho\, h\, \frac{t}{d}\right) + k_2\right]\varphi_0 \qquad (1)$$

where h (increasing downwards) is height (in m), $\Delta\rho$ is the density contrast between crystals and melt (1880 kg m^{-3} for chromite and 420 kg m^{-3} for olivine), t is time (in seconds), d is grain size (in m), and φ_0 is the porosity (volume fraction) after crystal settling. The parameters k_1 and k_2 are experimentally determined constants and are –0·0581 and 2·50 for chromite, and –0·119 and 3·88 for olivine. In the absence of experiments for other silicates, we take the values for olivine as representative for other mafic silicates and specifically for orthopyroxene, which is dominant in our silicate cumulates.

We have applied the above model to the sequence from the UG2 chromitite layer to the top of the UG3 hanging-wall pyroxenite (from 236·8 m core depth to 221·5 m; Fig. 11). This corresponds to 0·7 m UG2

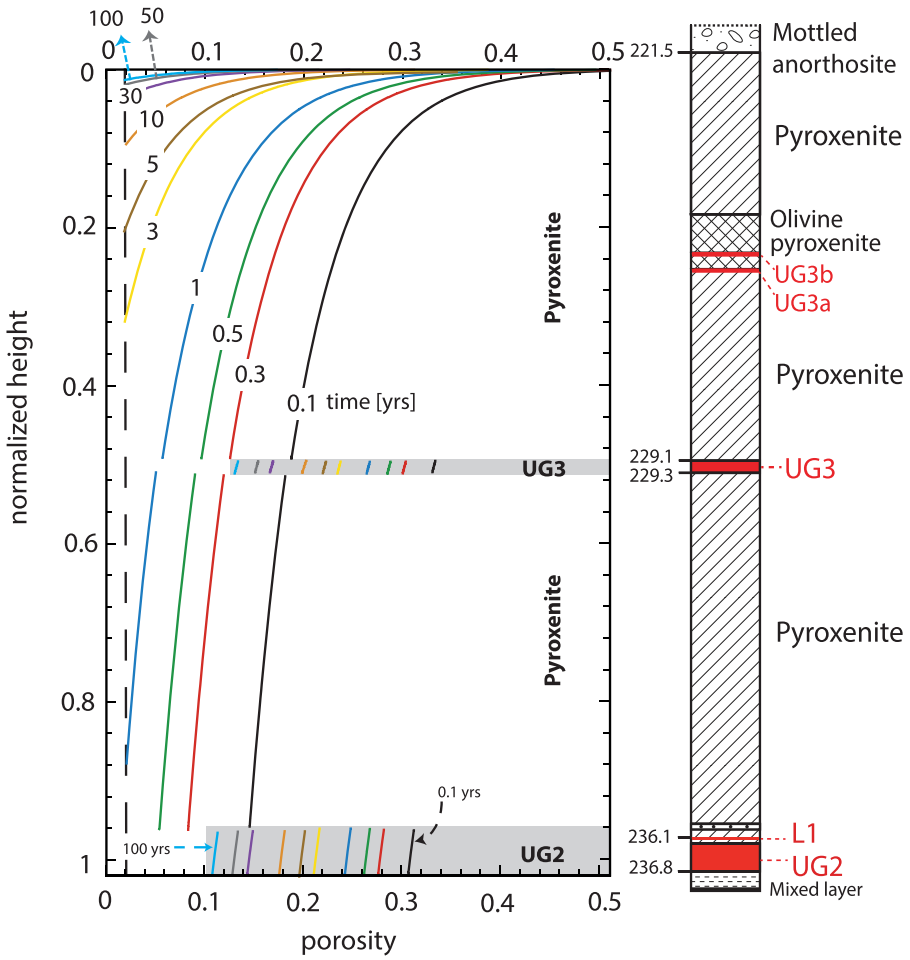

Fig. 11. Evolution of porosities with increasing time (labels on each line, in years) in a multilayer sequence similar to the studied drill core. For this calculation an average grain size of 0·2 mm and 2 mm is considered for the chromitites and pyroxenites, respectively. Compaction limit is set to 0·02 porosity (dashed line).

chromitite, 6·8 m pyroxenite (including thin layers at the top of UG2) between UG2 and UG3, 0·2 m UG3 chromitite and 7·6 m pyroxenite as a top layer. The observed average grain sizes are 0·2 mm and 2 mm for the chromitites and pyroxenites, respectively. From our experiments on the gravitational settling of olivine and chromite an initial porosity of 0·51(2) for both olivine and chromite was assumed as the starting point of our model. Additionally, we have augmented the initial crystal pile height such that the final height corresponds to the observed one.

Time scale of compaction

Chromite layer formation

Two main models exist for the formation of the chromitite layers. Either the chromite is transported from some deeper level and injected into the Bushveld magma chamber together with a more primitive melt (e.g. Eales, 2000; Mondal & Mathez, 2007; Voordouw & Beukes, 2009) or it crystallized *in situ* within the magma chamber, possibly as a result of pressure fluctuations (e.g. Cameron, 1977, 1980; Lipin, 1993; Cawthorn, 2005) or because of an increase in oxygen fugacity (Ulmer, 1969; Cameron & Desborough, 1969). In either case formation of major chromitite layers most probably requires injection of a more primitive magma, which moves the resident magma away from the silicate mineral saturation surface, either in temperature, pressure or compositional space. Irvine (1977) proposed that injection of a more primitive magma and mixing with the resident magma (which may or may not have assimilated country rock) removes the resulting melt, at least temporarily, from the chromite–olivine or chromite–opx cotectic into the liquidus field of chromite, requiring a minimal increase in the temperature of the Bushveld magma chamber. A small amount of cooling would then again lead to opx saturation. Whether the chromite forming the chromitite layers had been sinking directly from the magma chamber or had also been laterally displaced by density currents (e.g. Maier & Barnes, 2008) is debated; however, independent of the deposition mechanism, an initial porosity of ~50 vol. % holds.

Single layer compaction

If the chromite was transported from a deeper magma chamber, chromite settling would occur almost

instantaneously. The compaction time scale for such a single chromitite layer may then be used to determine the time span until the magma chamber had cooled enough to become saturated again in opx (or olivine + opx above UG3). Both UG2 and UG3 are underlain by opx cumulates, testifying to opx saturation before chromitite formation.

Experimental compaction of chromite is efficient only in monomineralic layers, the formation of a few per cent of olivine or opx leading to an exponential decrease in compaction velocity (Manoochehri & Schmidt, 2014). In such experiments, compaction of chromitite from an initial porosity of 0·51 to 0·4 is 100 times slower in the presence of olivine or opx than in the monomineralic case, and compaction to 0·3 is ~40 000 times slower. Although these rates have considerable errors, it is safe to assume that crystallization of silicates in the chromitite layer would slow down compaction by orders of magnitude. When the opx layer formed on top of the chromitite, the interstitial melt in the chromitite would saturate in opx. Based on the approximation that chromitite compaction is effectively halted when opx begins to crystallize, the compaction time for a single chromitite layer becomes a proxy for the maximum time between the chromite and opx layer deposition. The time to compact UG2 or UG3 from an initial porosity of 0·51 (as achieved by sedimentation) to the observed porosity of ~0·25 or ~0·4, as deduced from the silicate fraction, amounts to ~3 years for UG2 and ~0·1 years for UG3 [calculated using equation (1)].

Following the deposition of the hanging-wall opx layer of UG2 or UG3, compaction to porosities of ~0·11 and ~0·13 occurs at the base of their respective 6·8 m and 3·5 m thick hanging-wall pyroxenites. The compaction times for these single layers are 0·5 and 0·7 years, respectively. This time might be taken as either (1) the period of cooling until the next injection of more primitive magma leads to chromite saturation only, or (2) the period of cooling that leads to crystallization of plagioclase in the interstitial melt, which again may effectively shut down compaction. For this latter case, a norite layer would be expected above the pyroxenites.

After deposition of two more chromitite layers (i.e. UG3a and UG3b of 8 and 6 cm thickness) the UG3b hanging-wall pyroxenite of 3·5 m thickness was formed. This layer is compacted to a porosity that is on average 0·19 in its lower part, which requires about 0·3 years.

Altogether, the compaction times of the layers add up to <10 years. If the onset of formation of each new layer directly follows the formation of the previous layer, then this is the total time span involved in the formation of the UG2–UG3 cumulate package.

Concomitant compaction of the UG2–UG3 crystal pile

At the other extreme the entire UG2–UG3 cumulate section may be considered as depositing faster than any compaction process. This would require the injection of fresh magmas to occur on a time scale much shorter than the compaction process. We have calculated the compaction of the entire 20 m section of cumulates (neglecting the thin UG3a and UG3b chromitites). Figure 11 shows the porosities developing in these layers over a time interval of 0·1–100 years. The observed porosity reduction is much faster in the silicate layers, such that after 1 year the lower part of the pyroxenite layer reaches the compaction limit (i.e. 0·02 porosity). With increasing time this compaction limit moves upwards and after 100 years the uppermost layer has reached the compaction limit. In the chromitite layers porosity reduction is slower and porosity in UG2 develops to the present values (~0·2) within 1–5 years. The starting point of this calculation is a situation where all crystals that now form the UG2–UG3 pyroxenite–chromitite package have settled. Under these conditions, the calculated paleo-porosities are reached after 1 year, suggesting that the entire UG2–UG3 layer package may have formed on this time scale (i.e. rather fast for geological processes).

The time scale of cumulate formation versus cooling

The dominantly concordant character of the layering in large mafic layered intrusions suggests that a magma chamber has been present during the entire lifetime of these depositional magmatic systems. Below, we argue that temperature variations in the magma chamber during the formation of the Critical Zone in the Bushveld may have been rather limited and not more than a few tens of degrees centigrade.

The temperature range during the formation of the UG2–UG3 cumulate section

Below the UG2–UG3 cumulate section there is >20 m of norite. To deposit and conserve the cumulates in a planar fashion, these norites should be well consolidated at the time of chromite deposition. Deposition of the pyroxenites then requires temperatures above plagioclase saturation, and deposition of the chromitites requires temperatures above opx (+cpx) saturation. Irvine (1970*a*) pointed out that the Bushveld parent magma was probably very close to the plagioclase–opx(–cpx) cotectic, allowing for a rapid change of crystallization sequence with pressure or, by analogy, with small changes in magma composition. Helz (1995), on the basis of experiments on a likely Stillwater parent magma composition, suggested that there is only 30–50°C difference between opx-in (~1200°C) and plagioclase-in. Inspection of experimentally determined phase diagrams for the system CaO–MgO–Al_2O_3–SiO_2 (CMAS) on the plagioclase–opx cotectic reveals that at 1 atm this cotectic extends from the olivine–plagioclase–olivine peritectic point at 1260°C to the plagioclase–opx–quartz eutectic at 1220°C (Andersen, 1915). Tilley *et al.* (1968) found that a chilled margin bronzite gabbro from the Muskox intrusion has olivine, opx, cpx and

plagioclase appearing (in this sequence) within 30°C, between 1205°C and 1177°C, whereas a hypersthene gabbro from the Bushveld had plagioclase, opx and cpx appearing within 20°C, from 1195 to 1173°C. A norite from a quenched sill margin in the Bushveld crystallized all four phases, olivine, opx, cpx and plagioclase within 16°C (Cawthorn & Davies, 1983). At 10 kbar, in CMAS, the plagioclase–opx cotectic intersects the spinel field at its upper temperature end at 1370°C and terminates at 1350°C in the plagioclase–opx–quartz eutectic (Sen & Presnall, 1984). Longhi and co-workers (Vander Auwera *et al.*, 1998; Longhi *et al.*, 1999) emphasized that in natural systems the olivine–plagioclase–olivine peritectic moves with pressure away from the quartz corner such that a thermal maximum develops on this cotectic at 5 kbar. The experiments of Longhi *et al.* (1999) suggest that at 11·5 kbar the branch of the opx–plagioclase cotectic between the thermal maximum and the spinel–opx–plagioclase peritectic extends over ~20°C only. Independent support for small temperature differences comes from plagioclase–pyroxene REE geothermometry, which indicates only 30°C variation in the Upper Critical Zone of the Bushveld (Sun *et al.*, 2013).

In conclusion, we follow Irvine (1970*a*), arguing that the rapid change of the relative crystallization sequences of opx and plagioclase (and cpx in other LMIs) requires the bulk magma to be close to the plagioclase–opx cotectic. If this is correct, then a temperature increase of as little as 10°C may remove the magma from saturation in opx, (cpx) and plagioclase, allowing for chromite saturation by the injection of only a modest amount of more primitive magma. In contrast, only 20–30°C cooling might be necessary to reach the plagioclase–opx–(cpx)–qz eutectic and hence (almost) complete solidification. Based on these arguments, we conclude that the temperature variations within the UG2–UG3 cumulate section were at most a few tens of degrees.

Cooling time scale

To model the cooling time scales of the Bushveld magma chamber, the thickness of the magma chamber and the injection rate of fresh magma at any given time would be needed. Fortunately, the cooling of relatively thin single layers requires assumptions about only the magma and lower boundary temperature, assuming that the magma chamber is large compared with the layer of interest. Assuming a magma temperature of 1200°C and a temperature of 900–1050°C for the norite at the base of the UG2–UG3 cumulate pile, 0·6–11 years are necessary to cool the 20 m cumulate by 10–50°C. A magma temperature of 1100°C would prolong this time by a factor of two. These cooling times are in the same range as the compaction times and, accepting the small temperature differences argued above, it is reasonable that compaction may exceptionally lead to porosities at the compaction limit of less than a few per cent; however, more often compaction may be slowed down substantially by the crystallization of additional phases.

Expulsion of interstitial liquid during compaction

Compaction could be limited by the accompanying decrease in permeability, which results in increasingly difficult extraction of the interstitial melt, ultimately hindering the upward percolation of this melt. The porosity at which the upward flow of melt becomes obstructed by the crystals can be calculated by equating the hydraulic pressure gradient (driving melt expulsion) with the effective pressure gradient resulting from the crystal pile. Using the observed grain sizes, the observed thicknesses of the layers, the residual melt fraction determined from the incompatible trace elements, the calculated compaction rates (detailed above), and an appropriate melt viscosity of 17 Pa s, the upward directed hydraulic gradient resulting from the rising melt is generally 1–2 orders of magnitude lower than the downward directed lithostatic gradient resulting from the crystal pile [equations (12) and (13) of Manoochehri & Schmidt (2014)]. With progressive compaction these two forces may become similar in the uppermost decimeter of the crystal pile where the melt flux is highest but compaction has already reduced porosity (and hence permeability). Expulsion of interstitial liquid is hence not a problem in the investigated 20 m section, at least as long as there is no intra-cumulus crystallization.

Permeabilities as a function of porosity reduction in the cumulate section (assuming a constant grain size for each layer) have been calculated and are shown in Fig. 12. At the beginning of the compaction process (<1·0 year), the chromitite layers have a much lower permeability in comparison with the pyroxenite layers, mostly owing to the finer grain size of the former. Because of the faster porosity reduction in the silicate layers, after 1 year of compaction, the permeability in the lowermost part of the pyroxenites reduces to that of the chromitite layers. Progressing further, the compaction limit is reached and, without grain maturation (not included in the model), permeabilities remain constant and are determined by the shutdown porosity (Fig. 12).

The chromitites as permeability barriers

The observation that expelled residual melts from lower cumulate layers accumulate at the bottom of chromitites in the form of footwall pegmatites suggests that at the time of this residual liquid expulsion, the chromitites were significantly less permeable than the underlying pyroxenites. However, our calculations suggest relatively small differences in permeability for compaction times >1 year, and these differences do not justify a relative impermeability of the chromite layer. Nevertheless, the permeability of the chromitite layers has been calculated considering only the cumulus chromite. If we consider that the observed large oikocrystic post-cumulus opx in the chromitites may grow during

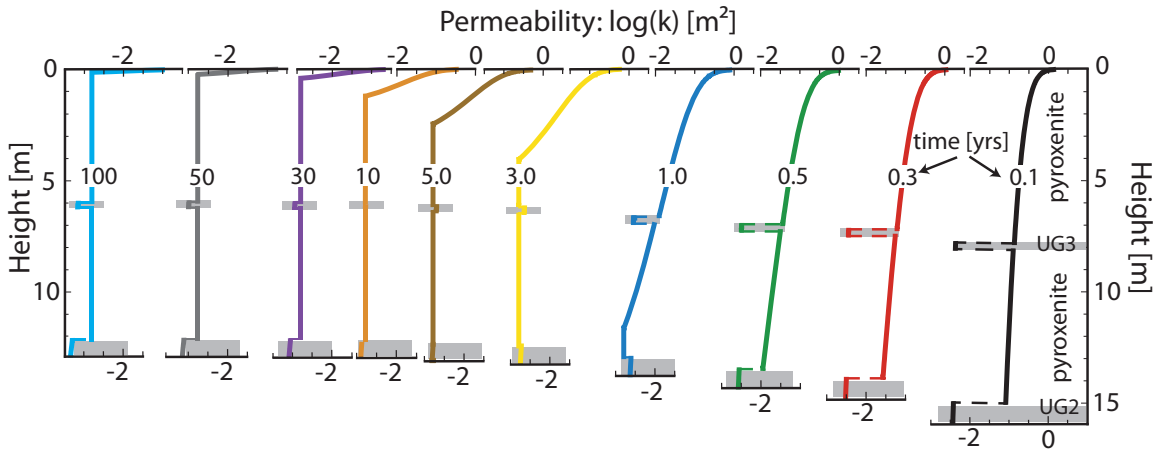

Fig. 12. Evolution of permeability with time in a multilayer sequence similar to the studied drill core. For permeability calculations, grain size is considered constant and identical to the values used for calculation of porosities (i.e. 0·2 mm and 2 mm for chromitite and pyroxenite units, respectively). After 1 year the initially lower permeabilities in chromitites are compensated by the faster porosity reduction in silicate layers so that the permeability in the lowermost part of the pyroxenite catches up.

continuing compaction, at least in the pyroxenite layers, the porosities and hence permeabilites would be much more reduced. As argued above, as soon as the pyroxenite layer on top of the chromitites begins to deposit, the interstitial liquid in the chromitites should saturate and crystallize opx that (1) reduces permeability, (2) slows down further compaction in the chromitites, and (3) more importantly in this context, shuts down the permeability such that the chromitites may effectively become permeability barriers.

CONCLUSIONS

The feasibility of compaction to the observed paleo-porosities of 0·06–0·41 for an almost 20 m sequence of cumulate rocks, extending from the pyroxenites underlying the UG2 chromitite to the hanging-wall pyroxenites of UG3 in the Bushveld Complex, has been investigated and modeled in this study. By quantifying the compaction time scales for such a profile, we calculate that gravitationally driven chemical compaction takes place within years to decades; this length of time should encompass the entire formation of the UG2–UG3–pyroxenite cumulate package. The porosities observed can easily develop without additional overload. The swiftness of the compaction process leads to the conclusion that compaction is probably limited by partial crystallization of the interstitial liquid through cooling, and that cooling of only a few degrees may be required.

Paleo-porosities, calculated from incompatible trace element concentrations, confirm the occurrence of enriched zones in the footwalls of the chromitites. These enriched zones, manifested by the footwall pegmatoids, are consistent with a collection of interstitial melts from the underlying compacting pyroxenites. Chromitite layers have apparently acted as permeability barriers for further upward percolation of these melts, with opx crystallization during compaction probably lowering the permeability of the chromitite layers. The redistribution of the interstitial melts during compaction fully accounts for the geochemical variations within the profile.

ACKNOWLEDGEMENTS

We are grateful to the Modikwa Platinum Mine for providing access to the drill cores. We also thank Moris J. Viljoen and Roger N. Scoon for their company during the field trip to South Africa and very helpful discussions about the Bushveld Complex. We thank J. VanTongeren for reviewing a pre-submission version of this paper, and A. Boudreau, C. Tegner, and I. Veksler for reviews. Nico Kueter is thanked for his help in XRF and LA-ICP-MS analysis.

FUNDING

SM benefited from a Marie Heim-Voegtlin (MHV) grant (# PMCDP2_129181) of the Swiss National Science Foundation (SNF) in the early stage of this project.

SUPPLEMENTARY DATA

Supplementary data for this paper are available at *Journal of Petrology* online.

REFERENCES

Andersen, O. (1915). The system anorthite–forsterite–silica. *American Journal of Science, Series 4* **39**(**232**), 407–454.

Ballhaus, C. G. & Stumpfl, E. F. (1985). Occurrence and petrological significance of graphite in the Upper Critical Zone, western Bushveld Complex, South Africa. *Earth and Planetary Science Letters* **74**, 58–68.

Barnes, S. (1986). The effect of trapped liquid crystallization on cumulus mineral compositions in layered intrusions. *Contributions to Mineralogy and Petrology* **93**, 524–531.

Barnes, S. J. & Campbell, I. H. (1988). Role of late magmatic fluids in Merensky-type platinum deposits: A discussion. *Geology* **16**, 488–491.

Barnes, S.-J. & Maier, W. D. (2002). Platinum-group element distributions in the Rustenburg layered suite of the Bushveld Complex, South Africa. The geology, geochemistry, mineralogy and mineral beneficiation of platinum-group elements. *Canadian Instotute of Mining, Metallurgy and Petroleum Special Volume* **54**, 431–458.

Barnes, S. J., Maier, W. D. & Curl, E. A. (2010). Composition of the marginal rocks and sills of the Rustenburg Layered Suite, Bushveld Complex, South Africa: implications for the formation of the platinum-group element deposits. *Economic Geology* **105**, 1491–1511.

Beattie, P. (1993). The generation of uranium series disequilibria by partial melting of spinel peridotite: constraints from partitioning studies. *Earth and Planetary Science Letters* **117**, 379–391.

Beattie, P. (1994). Systematics and energetics of trace-element partitioning between olivine and silicate melts: Implications for the nature of mineral/melt partitioning. *Chemical Geology* **117**, 57–71.

Bédard, J. H. (2006). Trace element partitioning in plagioclase feldspar. *Geochimica et Cosmochimica Acta* **70**, 3717–3742.

Boorman, S., McGuire, J., Boudreau, A. & Kruger, J. (2003). Fluid overpressure in layered intrusions: formation of a breccia pipe in the Eastern Bushveld Complex, Republic of South Africa. *Mineralium Deposita* **38**, 356–369.

Boorman, S., Boudreau, A. & Kruger, F. J. (2004). The Lower Zone–Critical Zone transition of the Bushveld Complex: a quantitative textural study. *Journal of Petrology* **45**, 1209–1235.

Boudreau, A. E. & McBirney, A. R. (1997). The Skaergaard layered series. 3. Non-dynamic layering. *Journal of Petrology* **38**, 1003–1020.

Boudreau, A. E., Mathez, E. A. & McCallum, I. S. (1986). Halogen geochemistry of the Stillwater and Bushveld complexes: evidence for transport of the platinum-group elements by Cl-rich fluids. *Journal of Petrology* **27**, 967–986.

Cameron, E. N. (1977). Chromite in the central sector of the eastern Bushveld Complex, South Africa. *American Mineralogist* **62**, 1082–1096.

Cameron, E. N. (1980). Evolution of the Lower Critical Zone, central sector, eastern Bushveld Complex, and its chromite deposits. *Economic Geology* **75**, 845–871.

Cameron, E. N. & Desborough, G. A. (1969). Occurrence and characteristics of chromite deposits—Eastern Bushveld Complex. In: Wilson, H. D. B. (ed.) *Magmatic Ore Deposits. Economic Geology Monograph* **4**, 23–40.

Campbell, I. H. (1978). Some problems with the cumulus theory. *Lithos* **11**, 311–323.

Cawthorn, R. G. (2005). Pressure fluctuations and the formation of the PGE-rich Merensky and chromitite reefs, Bushveld Complex. *Mineralium Deposita* **40**, 231–235.

Cawthorn, R. G. (2007). Cr and Sr: Keys to parental magmas and processes in the Bushveld Complex, South Africa. *Lithos* **95**(**3–4**), 381–398.

Cawthorn, R. G. & Barry, S. D. (1992). The role of intercumulus residua in the formation of pegmatoid associated with the UG2 chromitite, Bushveld Complex. *Australian Journal of Earth Sciences* **39**, 263–276.

Cawthorn, R. G. & Boerst, K. (2006). Origin of the pegmatitic pyroxenite in the Merensky Unit, Bushveld Complex, South Africa. *Journal of Petrology* **47**, 1509–1530.

Cawthorn, R. G. & Davies, G. (1983). Experimental data at 3 kbars pressure on parental magma to the Bushveld Complex. *Contributions to Mineralogy and Petrology* **83**(**1–2**), 128–135.

Cawthorn, G. & Walsh, K. L. (1988). The use of phosphorus contents in yielding estimates of the proportion of trapped liquid in cumulates of the Upper Zone of the Bushveld Complex. *Mineralogical Magazine* **52**, 81–89.

Cawthorn, R. G. & Webb, S. J. (2001). Connectivity between the western and eastern limbs of the Bushveld Complex. *Tectonophysics* **330**(**3–4**), 195–209.

Cousins, C. A. & Feringa, G. (1964). The chromite deposits of the Western belt of the Bushveld Complex. In: Haughton, S. H. (ed.) *The Geology of some Ore Deposits in Southern Africa,* Vol. 2. Geological Society of South Africa, pp. 183–202.

Deer, W. A., Howie, R. A. & Zussman, J. (1992). *An Introduction to the Rock-forming Minerals*. Pearson.

Eales, H. V. (1987). *Evolution of Chromium Ore Fields*. Van Nostrand Reinhold.

Eales, H. V. (2000). Implications of the chromium budget of the Western Limb of the Bushveld Complex. *South African Journal of Geology* **103**, 141–150.

Eales, H. V. & Cawthorn, R. G. (1996). The Bushveld Complex. In: Cawthorn, R. G. (ed.) *Developments in Petrology,* Volume 15. Elsevier, pp. 181–229.

Frei, D., Liebscher, A., Franz, G., Wunder, B., Klemme, S. & Blundy, J. (2009). Trace element partitioning between orthopyroxene and anhydrous silicate melt on the lherzolite solidus from 1·1 to 3·2 GPa and 1,230 to 1,535°C in the model system Na_2O–CaO–MgO–Al_2O_3–SiO_2. *Contributions to Mineralogy and Petrology* **157**, 473–490.

Godel, B., Barnes, S.-J. & Maier, W. D. (2011). Parental magma composition inferred from trace element in cumulus and intercumulus silicate minerals: An example from the Lower and Lower Critical Zones of the Bushveld Complex, South Africa. *Lithos* **125**(**1–2**), 537–552.

Guillong, G. A., Meier, D. L., Allan, M. M., Heinrich, C. A. & Yardley, B. W. D. (2008). SILLS: A MATLAB-based program for the reduction of laser ablation ICP-MS data of homogeneous materials and inclusions. *Mineralogical Association of Canada Short Course* **40**, 328–333.

Hatton, C. J. & von Gruenewaldt, G. (1987). In: Stowe, C. W. (ed.) *Evolution of Chromium Ore Fields*. New York: Van Nostrand Reinhold, pp. 109–143.

Helz, R. T. (1995). The Stillwater Complex, Montana: a subvolcanic magma chamber? *American Mineralogist* **80**(**11–12**), 1343–1346.

Henderson, P. (1968). The distribution of phosphorus in the early and middle stages of fractionation of some basic layered intrusions. *Geochimica et Cosmochimica Acta* **32**, 897–911.

Henderson, P. (1970). The significance of the mesostasis of basic layered igneous rocks. *Journal of Petrology* **11**, 463–473.

Hulbert, L. J. & von Gruenewaldt, G. (1985). Textural and compositional features of chromite in the lower and critical zones of the Bushveld Complex south of Potgietersrus. *Economic Geology* **80**, 872–895.

Hunter, R. H. (1996). Texture development in cumulate rocks. In: Cawthorn, R. G. (ed.) *Layered Intrusions. Developments in Petrology,* Volume 15. Elsevier, pp. 77–101.

Irvine, T. N. (1970a). Crystallization sequence in the Muskox intrusion and other layered intrusions, I. *Olivine–pyroxene–plagioclase relations. Geological Society of South Africa, Special Publication* **1**, 441–476.

Irvine, T. (1970b). Heat transfer during solidification of layered intrusions. I. Sheets and sills. *Canadian Journal of Earth Sciences* **7**, 1031–1061.

Irvine, T. N. (1977). Origin of chromitite layers in the Muskox intrusion and other stratiform intrusions: A new interpretation. *Geology* **5**, 273–277.

Irvine, T. N. (1982). Terminology for layered intrusions. *Journal of Petrology* **23**, 127–162.

Jordan, T. H. (1979). Mineralogies, densities and seismic velocities of garnet lherzolites and their geophysical implications. In: Boyd, F. R. & Meyer, H. O. A. (eds) *The Mantle Sample: Inclusion in Kimberlites and Other Volcanics*. American Geophysical Union, pp. 1–14.

Klerk, W. J. (1995). Textures exhibited by feldspars in the Giant Mottled Anorthosite (GMA) of the bastard unit in the Upper Critical Zone, Western Bushveld Complex. *Mineralogy and Petrology* **54**(**1–2**), 25–34.

Lipin, B. R. (1993). Pressure increases, the formation of chromite seams, and the development of the Ultramafic Series in the Stillwater Complex, Montana. *Journal of Petrology* **34**, 955–976.

Longhi, J., Vander Auwera, J., Fram, M. S. & Duchesne, J.-C. (1999). Some phase equilibrium constraints on the origin of Proterozoic (massif) anorthosites and related rocks. *Journal of Petrology* **40**, 339–362.

Maier, W. & Barnes, S. J. (2008). Platinum-group elements in the UG1 and UG2 chromitites, and the Bastard reef, at Impala platinum mine, western Bushveld Complex, South Africa: Evidence for late magmatic cumulate instability and reef constitution. *South African Journal of Geology* **111**(**2–3**), 159–176.

Maier, W. D., Barnes, S. J. & Groves, D. I. (2013). The Bushveld Complex, South Africa: formation of platinum–palladium, chrome- and vanadium-rich layers via hydrodynamic sorting of a mobilized cumulate slurry in a large, relatively slowly cooling, subsiding magma chamber. *Mineralium Deposita* **48**, 1–56.

Manoochehri, S. & Schmidt, M. (2014). Settling and compaction of chromite cumulates employing a centrifuging piston cylinder and application to layered mafic intrusions. *Contributions to Mineralogy and Petrology* **168**, 1–20.

Mathez, E. A. & Mey, J. L. (2005). Character of the UG2 chromitite and host rocks and petrogenesis of its pegmatoidal footwall, northeastern Bushveld Complex. *Economic Geology* **100**, 1617–1630.

Mathez, E. A., Hunter, R. H. & Kinzler, R. (1997). Petrologic evolution of partially molten cumulate: the Atok section of the Bushveld Complex. *Contributions to Mineralogy and Petrology* **129**, 20–34.

McKenzie, D. (1984). The generation and compaction of partially molten rock. *Journal of Petrology* **25**, 713–765.

Meurer, W. P. & Boudreau, A. E. (1996). **Compaction of density-stratified cumulates: effect on trapped-liquid distribution. *Journal of Geology* **104**, 115–120.

Meurer, W. P. & Boudreau, A. E. (1998a). Compaction of igneous cumulates Part I: Geochemical consequences for cumulates and liquid fractionation trends. *Journal of Geology* **106**, 281–292.

Meurer, W. P. & Boudreau, A. E. (1998b). Compaction of igneous cumulates Part II: Compaction and the development of igneous foliations. *Journal of Geology* **106**, 293–304.

Meurer, W. P. & Meurer, M. E. S. (2006). Using apatite to dispel the 'trapped liquid' concept and to understand the loss of interstitial liquid by compaction in mafic cumulates: an example from the Stillwater Complex, Montana. *Contributions to Mineralogy and Petrology* **151**, 187–201.

Mondal, S. K. & Mathez, E. A. (2007). Origin of the UG2 chromitite layer, Bushveld Complex. *Journal of Petrology* **48**, 495–510.

Naldrett, A. J., Gasparrini, E. C., Barnes, S. J., von Gruenewaldt, G. & Sharpe, M. R. (1986). The upper critical zone of the Bushveld Complex and the origin of Merensky-type ores. *Economic Geology* **81**, 1105–1117.

Namur, O. & Charlier, B. (2012). Efficiency of compaction and compositional convection during mafic crystal mush solidification: the Sept Iles layered intrusion, Canada. *Contributions to Mineralogy and Petrology* **163**, 1049–1068.

Naslund, H. R. & McBirney, A. R. (1996). Mechanisms of formation of igneous layering. In: Cawthorn, R. G. (ed.) *Developments in Petrology*, Volume 15. Elsevier, pp. 1–43, http://dx.doi.org/10.1016/S0167-2894(96)80003-0.

Nicholson, D. M. & Mathez, E. A. (1991). Petrogenesis of the Merensky Reef in the Rustenburg section of the Bushveld Complex. *Contributions to Mineralogy and Petrology* **107**, 293–309.

Philpotts, A. R., Carroll, M. & Hill, J. M. (1996). Crystal-mush compaction and the origin of pegmatitic segregation sheets in a thick flood-basalt flow in the Mesozoic Hartford Basin, Connecticut. *Journal of Petrology* **37**, 811–836.

Philpotts, J. A. & Schnetzler, C. C. (1970). Phenocryst–matrix partition coefficients for K, Rb, Sr and Ba, with applications to anorthosite and basalt genesis. *Geochimica et Cosmochimica Acta* **34**, 307–322.

Prowatke, S. & Klemme, S. (2006). Trace element partitioning between apatite and silicate melts. *Geochimica et Cosmochimica Acta* **70**, 4513–4527.

SACS (South African Commission for Stratigraphy) (1980). Lithostratigraphy of the Republic of South Africa, South West Africa/Namibia and the Republics of Botswana, Transkei, and Venda. *Geological Survey of South Africa Handbook* **8**, 690.

Schmidt, M. W., Forien, M., Solferino, G. & Bagdassarov, N. (2012). Settling and compaction of olivine in basaltic magmas: an experimental study on the time scales of cumulate formation. *Contributions to Mineralogy and Petrology* **164**, 959–976.

Sen, G. & Presnall, D. C. (1984). Liquidus phase relationships on the join anorthite–forsterite–quartz at 10 kbar with applications to basalt petrogenesis. *Contributions to Mineralogy and Petrology* **85**, 404–408.

Sharpe, M. R. & Hulbert, L. J. (1985). Ultramafic sills beneath the eastern Bushveld Complex; mobilized suspensions of early lower zone cumulates in a parental magma with boninitic affinities. *Economic Geology* **80**, 849–871.

Shirley, D. N. (1987). Differentiation and compaction in the Palisades Sill, New Jersey. *Journal of Petrology* **28**, 835–865.

Sparks, R. S. J., Huppert, H. E., Kerr, R. C., McKenzie, D. P. & Tait, S. R. (1985). Postcumulus processes in layered intrusions. *Geological Magazine* **122**, 555–568.

Stolper, E. & Walker, D. (1980). Melt density and the average composition of basalt. *Contributions to Mineralogy and Petrology* **74**, 7–12.

Sun, C., Liang, Y., Ashwal, L. & VanTongeren, J. (2013). Temperature variations along stratigraphic height across the Bushveld complex with implications for magma chamber processes in layered intrusions. GSA Annual Meeting: 125th Anniversary of GSA, Denver, 27–30 October 2013.

Tegner, C., Thy, P., Holness, M. B., Jakobsen, J. K. & Lesher, C. E. (2009). Differentiation and compaction in the Skaergaard Intrusion. *Journal of Petrology* **50**, 813–840.

Tilley, C. E., Yoder, H. S. & Schairer, J. F. (1968). Melting relations of igneous rock series. *Carnegie Institution of Washington Yearbook* **66**, 450–457.

Ulmer, G. C. (1969). Experimental investigations of chromite spinels. In: Wilson, H. D. B. (ed.) *Magmatic Ore Deposits. Economic Geology Monograph* **4**, 114–131.

Vander Auwera J., Longhi, J. & Duchesne, J.-C. (1998). A liquid line of descent of the jotunite (hypersthene monzodiorite) suite. *Journal of Petrology* **39**, 439–468.

Van der Merwe J., & Cawthorn, R. G. (2005). Structures at the base of the Upper Group 2 chromitite layer, Bushveld Complex, South Africa, on Karee Mine (Lonmin Platinum). *Lithos* **83**, 214–228.

Veksler, I. V., Reid, D. L., Dulski, P., Keiding, J. K., Schannor, M., Hecht, L. & Trumbull, R. B. (2015). Electrochemical Processes in a Crystal Mush: Cyclic Units in the Upper Critical Zone of the Bushveld Complex, South Africa. *Journal of Petrology* **56**, 1229–1250.

Vermaak, C. F. (1976). The Merensky Reef; thoughts on its environment and genesis. *Economic Geology* **71**, 1270–1298.

Viljoen, M. J. & Scoon, R. N. (1985). The distribution and main geologic features of discordant bodies of iron-rich ultramafic pegmatite in the Bushveld Complex. *Economic Geology* **80**, 1109–1128.

Viljoen, M. J., De Klerk, W. J., Coetzer, P. M., Hatch, N. P., Kinloch, E. & Peyerl, W. (1986). The Union Section of Rustenburg Platinum Mines, with reference to the Merensky Reef. In: Anhaeusser, C. R. (ed.) *Mineral Deposits of Southern Africa,* Vol. 1. Geological Society of South Africa, pp. 1061–1090.

Villemant, B. (1988). Trace element evolution in the Phlegrean Fields (Central Italy): fractional crystallization and selective enrichment. *Contributions to Mineralogy and Petrology* **98**, 169–183.

Voordouw, R. J. & Beukes, N. J. (2009). Alteration and metasomatism of the UG2 melanorite and its stratiform pegmatoids, Bushveld Complex, South Africa—characteristics, timing and origins. *South African Journal of Geology* **112**, 47–64.

Vukmanovic, Z., Barnes, S., Reddy, S., Godel, B. & Fiorentini, M. (2013). Morphology and microstructure of chromite crystals in chromitites from the Merensky Reef (Bushveld Complex, South Africa). *Contributions to Mineralogy and Petrology* **165**, 1031–1050.

Wager, L. R. & Brown, G. M. (1968). *Layered Igneous Rocks*. Oliver & Boyd.

Wager, L. R., Brown, G. M. & Wadsworth, W. J. (1960). Types of igneous cumulates. *Journal of Petrology* **1**, 73–85.

Willmore, C. C., Boudreau, A. E. & Kruger, F. J. (2000). The halogen geochemistry of the Bushveld Complex, Republic of South Africa: implications for chalcophile element distribution in the Lower and Critical Zones. *Journal of Petrology* **41**, 1517–1539.